KeAi

CHINESE ROOTS
GLOBAL IMPACT

Contents lists available at ScienceDirect

Petroleum Science

journal homepage: www.keaipublishing.com/en/journals/petroleum-science



Original Paper

Systematic prediction of the gas content, fractures, and brittleness in fractured shale reservoirs with TTI medium



Yun Zhao a, b, Xiao-Tao Wen b, *, Chen-Long Li a, b, Yang Liu a, b, Chun-Lan Xie b

- ^a Key Laboratory of Earth Exploration and Information Techniques, Ministry of Education, Chengdu University of Technology, Chengdu, 610059, Sichuan,
- ^b College of Geophysics, Chengdu University of Technology, Chengdu, 610059, Sichuan, China

ARTICLE INFO

Article history:
Received 30 November 2023
Received in revised form
9 April 2024
Accepted 28 April 2024
Available online 1 May 2024

Edited by Meng-Jiao Zhou

Keywords:
Petrophysical modeling
Brittleness index
Fracture gas indication factor (GFI)
Tilted transversely isotropic (TTI)
Fracture density

ABSTRACT

The main objective is to optimize the development of shale gas-rich areas by predicting seismic sweet spot parameters in shale reservoirs. We systematically assessed the fracture development, fracture gas content, and rock brittleness in fractured gas-bearing shale reservoirs. To better characterize gas-bearing shale reservoirs with tilted fractures, we optimized the petrophysical modeling based on the equivalent medium theory. Based on the advantages of shale petrophysical modeling, we not only considered the brittle mineral fraction but also the combined effect of shale porosity, gas saturation, and total organic carbon (TOC) when optimizing the brittleness index. Due to fractures generally functioning as essential channels for fluid storage and movement, fracture density and fracture fluid identification factors are critical geophysical parameters for fractured reservoir prediction. We defined a new fracture gas indication factor (GFI) to detect fracture-effective gas content. A new linear PP-wave reflection coefficient equation for a tilted transversely isotropic (TTI) medium was rederived, realizing the direct prediction of anisotropic fracture parameters and the isotropic elasticity parameters from offset vector tile (OVT)domain seismic data. Synthetic seismic data experiments demonstrated that the inversion algorithm based on the LP quasinorm sparsity constraint and the split-component inversion strategy exhibits high stability and noise resistance. Finally, we applied our new prediction method to evaluate fractured gasbearing shale reservoirs in the Sichuan Basin of China, demonstrating its effectiveness.

© 2024 The Authors. Publishing services by Elsevier B.V. on behalf of KeAi Communications Co. Ltd. This is an open access article under the CC BY-NC-ND license (http://creativecommons.org/licenses/by-nc-nd/4.0/).

1. Introduction

In recent years, shale gas, an essential unconventional resource, has been widely researched in geophysical oil and gas exploration. Hydraulic fracturing is necessary to enhance production from low-porosity and poor-permeability shale (Wang et al., 2023; Pan et al., 2020). Generally, fractured gas-bearing shale reservoirs are characterized by crucial geophysical parameters such as fracture density, fluid type, and brittleness index. Accurate petrophysical modeling, the construction of fluid-sensitivity factors, and seismic inversion strategies are necessary to characterize these reservoirs properly (Xie et al., 2023; Qin et al., 2022).

E-mail address: wenxiaotao@cdut.cn (X.-T. Wen).

First, establishing suitable petrophysical models for fractured shale reservoirs is necessary for characterizing shale reservoirs. This petrophysical modeling bridges seismic elastic parameters and reservoir physical characteristics (Zeng et al., 2023; Yu et al., 2023; Zong et al., 2020; Zhang et al., 2015a). Shales typically have low permeability, low porosity, high brittleness, and high organic matter content. Under the assumption that heterogeneous rock is linear and elastic, the effective bulk modulus of isotropic rock can be calculated using the Voigt-Reuss-Hill average (Mavko et al., 2009; Hill, 1952; Reuss, 1929) and the isotropic self-consistent approximation (SCA) theory can effectively address rocks containing inclusions and minerals of different shapes (Budiansky, 1965; Yin et al., 2020). Considering poorly-connected pores containing immobile water in the rock, the Kuster-Toksöz (K-T) model (Kuster and Toksöz, 1974) determines the effective modulus of rocks containing inclusions of various shapes. Multiple theories exist for incorporating fractures into dry rock skeletons in fractured shale reservoirs. These theories can be classified into three main types:

^{*} Corresponding author. Key Laboratory of Earth Exploration and Information Techniques, Ministry of Education, Chengdu University of Technology, Chengdu, 610059, Sichuan, China.

seismic petrophysical theories that account for isolated pore fractures (Hudson, 1980), attenuated anisotropy (Pointer et al., 2000), and pore and seam connectivity at extreme frequencies (Thomsen, 1995).

The brittleness index represents the capacity of rock to fracture under external forces and serves as an essential parameter guiding hydraulic fracturing in shale (Oian et al., 2017; Zuo et al., 2023), In exploration geophysics, the elastic parameters of the rock, such as Young's modulus, Poisson's ratio, and the uniaxial compressive strength, are vital indicators of its brittleness. Additionally, the percentage content of brittle minerals in rock is equally crucial in determining rock brittleness. Brittle minerals such as quartz, feldspar, and calcite are more prone to fracture than less brittle minerals such as clay. Due to the complexity of geology, scholars have proposed various brittleness index expressions. Rickman et al. (2008) concluded that a higher Young's modulus and lower Poisson's ratio contribute to a higher brittleness, which provides the possibility of estimating rock brittleness by elastic parameters and makes it feasible to calculate Young's modulus and Poisson's ratio indirectly by utilizing the longitudinal and transverse wave velocities and density inverted in the isotropic seismic component. On this basis, Guo et al. (2012) investigated the relationship between rock brittleness and three elastic parameters, namely, Young's modulus, Lamé coefficient, and Poisson's ratio, and defined two brittleness indexes, namely, the ratio of Young's modulus to Poisson's ratio, and the ratio of P-wave modulus to the first Lamé coefficient, Later, Sharma and Chopra (2012) introduced a new brittleness index incorporating the product of the rock density and Young's modulus. In addition, the ratio of Young's modulus to the first Lamé coefficient was verified to be a new and effective indicator of the fracture capacity of rock by petrophysical modeling methods (Chen et al., 2014b). A new brittleness index that is more sensitive in low-porosity shales was constructed in combination with Poisson's ratio (Pan et al., 2020). Consequently, optimizing the brittleness index for a specific field is crucial for detecting the engineering sweet spots for shale gas.

Furthermore, offset vector tile (OVT)-domain seismic data consist of offset and azimuthal information, which not only enables isotropic seismic inversion but also effectively enables fracture parameter inversion based on the difference in seismic amplitudes in different directions induced by the fractures (Zhao et al., 2018; Luo et al., 2019; Chen et al., 2014a). Research on seismic anisotropy is primarily concerned with detecting fracture density and identifying different fracture fluids. To more precisely characterize the development of underground fractures, a range of linear PP-wave reflection coefficients for different fractured equivalent media have been derived based on the first-order perturbation theory (Jech and Pšenčik, 1989) and Born scattering theory (Shaw and Sen, 2004). These coefficients pertain to various mediums, including horizontal transversely isotropic (HTI) media, orthorhombic anisotropic (OA) media, and tilted transversely isotropic (TTI) media. Before performing anisotropic seismic inversion, fluid indicator factors are essential for fluid prediction, and numerous scholars have dedicated significant efforts to constructing fluid factors and studying fracture density from isotropic to anisotropic conditions (Smith, 2003; Chen et al., 2018; Pan and Zhang, 2018). Goodway et al. (1997) proposed an efficient method $(\lambda - \mu - \rho)$ for gas identification based on exploiting the anomalous stretching characteristics of subsurface formations. Based on a linear sliding model, Ge et al. (2020) studied the prediction method of fracture density and WA parameters for a monoclinic fractured medium based on Bayesian theory. Xue et al. (2017) proposed a new fluid factor expression and a matrix expression of the azimuthally anisotropic reflection amplitude and normal and tangential fracture weaknesses. They predicted the fracture density and new fluid factor by prestack PP-

wave amplitude variations with offset and azimuth (AVOAz) technology. Schoenberg and Sayers (1995) used the ratio of normal to shear compliance K_T/K_N as a widely used fracture fluid factor in anisotropic inversion. Although this method is indirect and may result in cumulative errors during the conversion process, it does provide insight into fracture weaknesses. It is significant in defining the fluid indication factor required for identifying the fracture fluid. In other words, developing methods for the direct seismic inversion of anisotropic fracture parameters is essential for improving the prediction of engineering and geological sweet spots for shale gas.

This article aims to systematically study rock brittleness estimation, fracture gas identification, and fracture density prediction for fractured gas-bearing shale reservoirs. By conducting the petrophysical simulations of shale reservoirs, we achieved a petrophysical method for preferring the brittleness index in terms of the mineral components while also considering the porosity, gas saturation, and organic matter content. We then define a susceptible fracture gas indication factor to derive a new PP-wave reflection coefficient for a TTI medium. Based on the inversion algorithm constrained by the LP quasinorm (Boyd et al., 2011; Euhanna et al., 2015; Zhao et al., 2023), the OVT-domain seismic data enable the inversion of elastic parameters through the isotropic seismic component and the fracture gas indication factor and fracture density through the anisotropic seismic component. Finally, systematic and practical predictions are achieved for the shale reservoirs of the Longmaxi-Wufeng formations in the Sichuan Basin. China.

2. Methodology

2.1. Fracture parameters and a new fracture gas indication factor

The linear-slip and Hudson thin-coin-shaped fracture models have the same first-order representation under the long-wavelength assumption. The relationship between the linear sliding model parameters and the fracture rock correlation parameters can be established by the Hudson model first-order equivalent elastic stiffness matrix (Schoenberg and Douma, 1998; Bakulin et al., 2000):

$$\delta_{\rm N} = \frac{4e}{3g^{\rm b}(1-g^{\rm b})\left[1 + \frac{1}{\pi(1-g^{\rm b})}\left(\frac{k_{\rm fluid} + \frac{4}{3}\mu_{\rm fluid}}{\mu^{\rm b}\chi_{\rm fracture}}\right)\right]} \tag{1}$$

$$\delta_{\mathrm{T}} = \frac{16e}{3\left(3 - 2g^{\mathrm{b}}\right)\left[1 + \frac{4}{\pi(3 - 2g^{\mathrm{b}})}\left(\frac{\mu_{\mathrm{fluid}}}{\mu^{\mathrm{b}}\chi_{\mathrm{fracture}}}\right)\right]} \tag{2}$$

where $\delta_{\rm N}$ and $\delta_{\rm T}$ denote the normal fracture weakness and tangential fracture weakness, respectively; $k_{\rm fluid}$ and $\mu_{\rm fluid}$ are the bulk modulus and shear modulus of the fracture fillings, respectively; e represents the fracture density; $g^{\rm b} = \mu^{\rm b}/M^{\rm b}$, $\mu^{\rm b}$ and $M^{\rm b}$ denote the P- and S-wave moduli of the surrounding rock, respectively; and $\chi_{\rm fracture}$ denotes the fracture aspect ratio.

Fig. 1 shows the normal fracture weakness with oil saturation S_0 in Fig. 1(a), and gas saturation S_g in Fig. 1(c), and the tangential fracture weakness with oil saturation in Fig. 1(b) and gas saturation in Fig. 1(d). Comparing Fig. 1(a) and (c), we can observe that the normal fracture weakness increases with increasing fluid saturation (S_0 and S_g), where it varies more with S_g . Fig. 1(b), (d) show that the tangential fracture weakness does not vary with fluid type or fluid saturation, so it can be concluded that the normal fracture

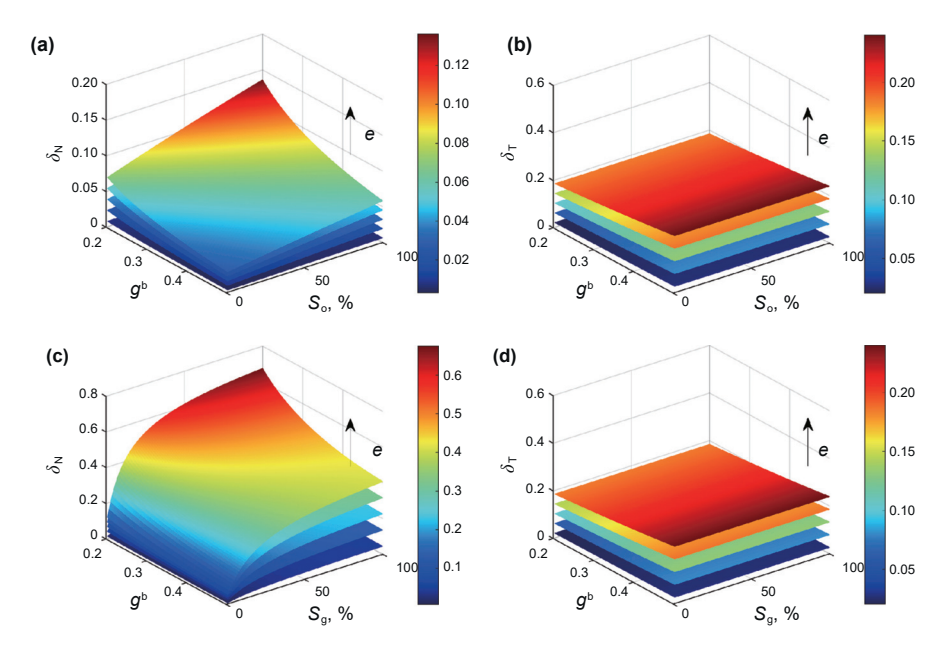


Fig. 1. The influence of different fluid types on fracture weaknesses, where (a) and (b) show the variations in the fracture normal and tangential weaknesses, respectively, with oil saturation, and (c) and (d) show the variation of fracture normal and tangential weaknesses, respectively, with gas saturation.

weakness is more sensitive to the fracture fluid. The tangential fracture weakness is independent of the fluid type and saturation conditions, and only the normal fracture weakness is sensitive to fracture fluids. Schoenberg and Sayers (1995) suggested an anisotropic fluid indicator, F_S , for the normal and tangential fracture compliance parameters.

$$F_{S} = \frac{Z_{N}}{Z_{T}} = g^{b} \frac{\delta_{N}(1 - \delta_{T})}{\delta_{T}(1 - \delta_{N})}$$

$$(3)$$

where $Z_{\rm N}$ and $Z_{\rm T}$ represent the normal and tangential fracture compliance parameters, respectively.

Considering that the fracture aspect ratio should be between 0.01 and 0.001, the fracture density is generally less than 0.1, etc., δ_N \ll 1 and δ_T \ll 1:

$$F_{\rm S} = g^{\rm b} \frac{\delta_{\rm N}}{\delta_{\rm T}} \tag{4}$$

We can eliminate the influence of any fluid on the tangential weakness, which is expressed as a direct relationship with the fracture density.

$$\delta_{\rm T} = \frac{16e}{3(3 - 2g^{\rm b})} \tag{5}$$

Based on Eqs. (4) and (5), we define a new fracture gas indication factor, *GFI*, considering that fracture fluid migration rather than fluid enrichment becomes feasible when the fractures are fully developed or relatively well developed, which is characterized by the following expression based on petrophysical parameters:

$$GFI = eF_{S} = \frac{\left(3 - 2g^{b}\right)e}{4(1 - g^{b})} \left[1 + \frac{1}{\pi(1 - g^{b})} \left(\frac{k_{\text{fluid}}}{\mu^{b} \chi_{\text{fracture}}}\right)\right]^{-1}$$
 (6)

Fig. 2 illustrates the analytical results of the parameter *GFI* for different fluid combination types and fracture aspect ratios, where S_0 denotes the oil saturation and S_g denotes the gas saturation. The directions of the black arrows in Fig. 2(a), (b) indicate the direction in which the fracture density increases. An increase in the

parameter *GFI* represents an increase in the effective bulk modulus of the fracture fluid. However, more significantly, the parameter *GFI* is almost insensitive to oil-water mixing fluids but highly sensitive to gas-water mixing fluids, and the parameter *GFI* is much more sensitive to fracture gas content than to fracture density. Moreover, the black arrow in Fig. 2(c) indicates the direction in which the fracture aspect ratio increases, but the parameter *GFI* also changes almost little with the fracture aspect ratio among the different gas saturation cases. The parameter *GFI* manifests much more sensitivity to the fracture gas content than to the fracture aspect ratio. Consequently, the parameter *GFI* can be considered as an effective fracture gas indicator in fractured gas-bearing reservoirs.

Based on the conclusions of the above analysis, with the hypothesis that the parameter *GFI* is little affected by the change in fracture density and the change in fracture aspect ratio, we determine a specific indication factor of the gas content in the fracture, which can be directly involved in the anisotropic seismic inversion. We present the detailed derivation in Section 2.3.

2.2. Optimization of the brittleness index for gas-bearing shale reservoirs based on rock physics

The brittleness index is an essential parameter for evaluating the accessibility of reservoir rocks for hydraulic fracturing, and the higher the brittleness index of shale is, the better the fracturing effect of the shale after fracturing. Due to the complexity of the underlying medium, various forms of brittleness index expressions have been proposed, so determining the optimum form of the brittleness index is critical. The primary forms are summarized in Table 1, where E represents Young's modulus, σ represents Poisson's ratio, ρ represents density, and λ represents the first Lamé constant. The subscripts max and min denote the maximum and minimum values, respectively.

To better characterize gas-bearing shale reservoirs, we establish a more suitable petrophysical modeling method as shown in Fig. 3. First, the effective elasticity modulus of an isotropic medium is calculated with VRH average (Mavko et al., 2009), and then, assuming the clay as the background, the self consistent approximation (SCA) model (Berryman, 1980, 1995) is used to add a lower

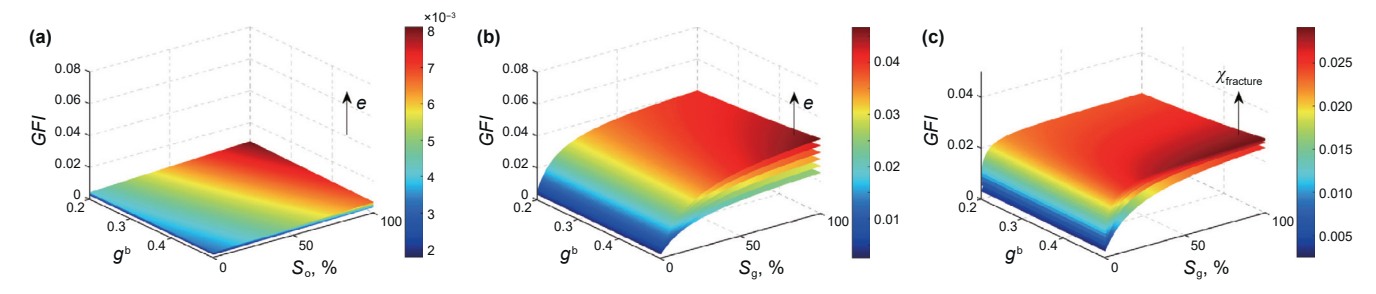


Fig. 2. Characterization of the variation in the parameter *GFI* with different fracture parameters and fluid saturations, where (a) shows the variation in oil saturation at different fracture densities varying from 0.01 to 0.09 by 0.02, (b) shows the variation in gas saturation at different fracture densities varying from 0.01 to 0.09 by 0.02, and (c) shows the variation in gas saturation at different fracture aspect ratios varying from 0.001 to 0.006 by 0.001.

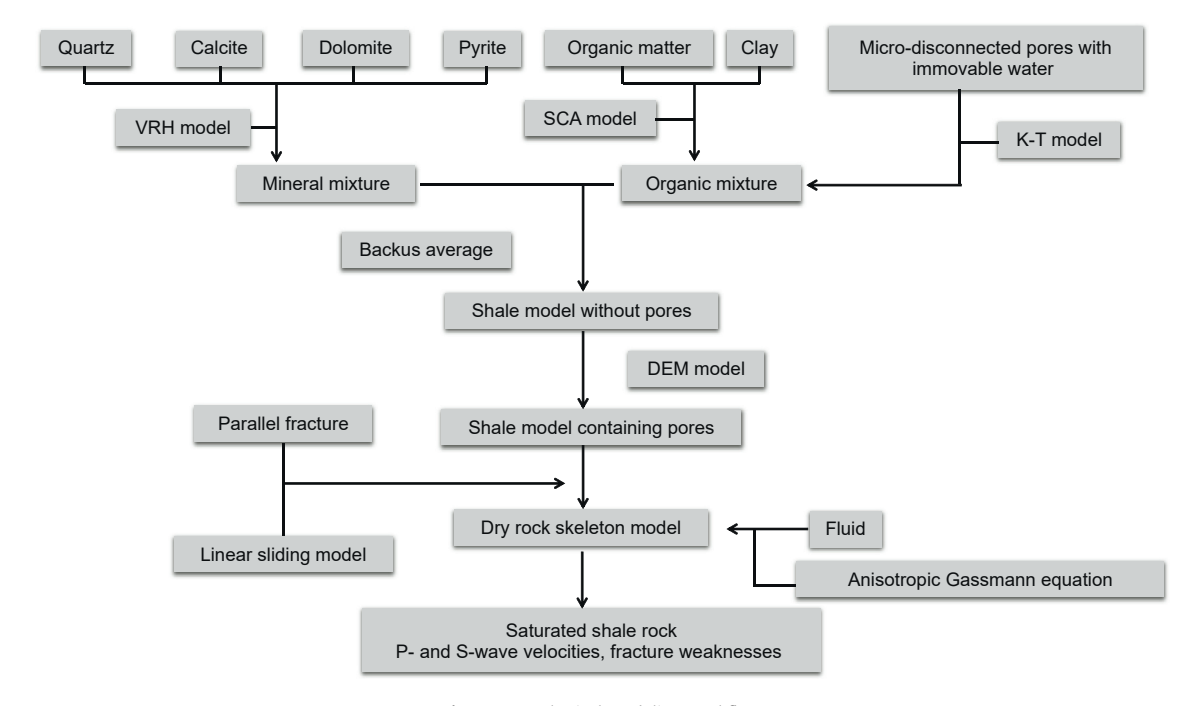
Table 1Expressions for five common brittleness indexes characterized by isotropic elastic parameters.

Brittleness index	Expression	
BI ₁ (Rickman et al., 2008)	$BI_1=(E_b+\sigma_b)/2$	(7)
	$E_{\rm b}=(E-E_{\rm min})/(E_{\rm max}-E_{\rm min})$	
	$\sigma_{\rm b} = (\sigma - \sigma_{\rm max})/(\sigma_{\rm min} - \sigma_{\rm max})$	
BI ₂ (Sharma and Chopra, 2012)	$BI_2 = E\rho$	(8)
BI ₃ (Guo et al., 2012)	$BI_3 = E/\sigma$	(9)
BI ₄ (Guo et al., 2012)	$BI_4 = M/\lambda$	(10)
BI ₅ (Chen et al., 2014b)	$BI_5 = E/\lambda$	(11)

organic matter content (kerogen as inclusions), and the K-T model (Kuster and Toksöz, 1974) was employed to add disconnected pores containing immoveable water (Zhang et al., 2015a, 2015b; Pan et al., 2020). Since the shale is distributed in layers, the equivalent stiffness matrix could be calculated as a layered equivalent background medium using Backus averaging (Backus, 1962). On this basis, the differential effective medium (DEM) model (Berryman, 1980) is used to add empty pore space to the rock mixture to obtain a dry rock skeleton. Fractured gas-bearing shale reservoirs require consideration of the effects of the fractures, and we utilized the linear sliding model (Schoenberg, 1980) to incorporate a set of

parallel fractures. Finally, the equivalent fluid for gas-water mixing calculated by the Wood equation (Wood and Lindsay, 1956) is added to the empty pores and fracture spaces using the anisotropic Gassmann equation (Brown and Korringa, 1975). This approach is used to estimate geophysical elasticity and fracture parameters via the equivalent modulus theory of an anisotropic rock skeleton saturated with different fluids.

Table 2 shows the bulk modulus K, S-wave modulus μ , and density ρ of different rock mineral fractions and fluids in Well A. Fig. 4 shows the logging curves of Well A in the research work area of this paper, which mainly include mineral content, MCC (quartz, dolomite, calcite, clay, pyrite, and organic matter), P- and S-wave velocities V_P and V_S , water saturation S_W , total porosity φ^t , and total organic carbon (TOC) content, in which the coupling degree of the P- and S-wave velocities on Well A and the predicted velocities of the rock physics model is utilized to verify the reasonableness and effectiveness of the modeling results. It is trustworthy that the relative error REP between the predicted P-wave velocity based on the petrophysical modeling in Fig. 4(d) and the logged P-wave velocity hardly exceeds 0.1, and the same quality is achieved for the Swave velocity REP in Fig. 4(e). Fig. 5 exhibits the relevant property parameters in the petrophysical modeling that are not used in the subsequent geophysical study of this paper.



 $\textbf{Fig. 3.} \ \ \text{Petrophysical modeling workflow}.$

Table 2Parameters related to the correlation model of fractured rock physical medium (Mayko et al., 2009).

Minerals and fluids	K, GPa	μ, GPa	ρ, g/cc
Quartz	37.0	44.0	2.65
Calcite	76.8	32.0	2.71
Pyrite	147	132	4.90
Dolomite	94.9	45.0	2.87
Clay	20.0	7.00	2.50
Organic matter	2.98	2.97	1.34
Gas	0.000130	0	0.000650
Brine	2.25	0	1.02

To optimize the brittleness index in this research, we consider not only the effect of traditional mineral fractions on rock brittleness but also the contributions of porosity, gas saturation, and organic matter to the brittleness index of fractured gas-bearing shale based on the advantages of microscopic petrophysical modeling methods.

First, we perform a preliminary screening of the effects of the brittle minerals (quartz, calcite, and dolomite) and their contents of Well A on the five brittleness indexes listed in Table 1. Due to the large order of magnitude differences among the brittleness indexes, the analytical procedure used is the normalized brittleness index. Quartz content (V-quartz), calcite content (V-calcite), and dolomite content (V-dolomite) vary from the ranges 32%-50%, 0-15%, and 0–21%, respectively. With increasing the content of brittle minerals (quartz, calcite, dolomite), the content of weakly brittle clay decreases by the same proportion as shown in Fig. 6. The different types of brittleness indexes exhibit the same positive correlation with the brittle mineral content. However, notably, the sensitivities of the same brittleness index to variations in different mineral contents are inconsistent. Therefore, it is necessary to quantitatively assess the degree of the contribution of the brittle mineral fraction to the brittleness indexes via Eq. (12).

$$MWS = 100\% \times \frac{\sum_{m=1}^{3} \sum_{n=1}^{n} [(BI_{n}^{m} - BI_{\min}^{m})V_{n}^{m}]}{\sum_{m=1}^{3} \sum_{n=1}^{n} V_{n}^{m}}$$
(12)

where MWS denotes the mineral component content weighted

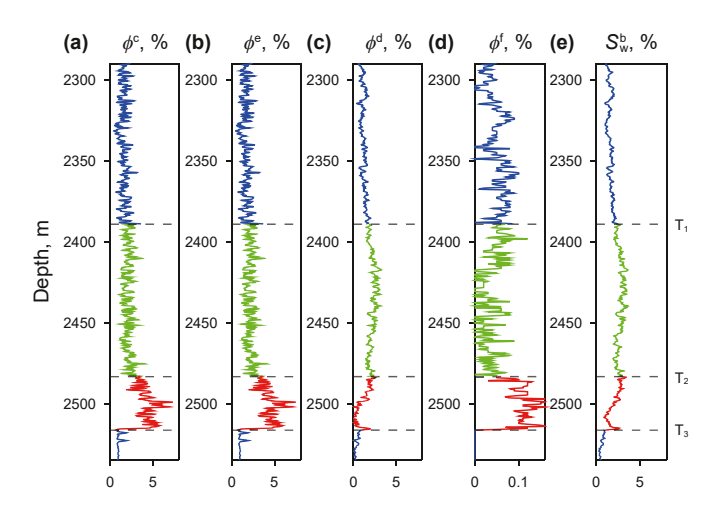


Fig. 5. Petrophysical modeling other relevant parameters on Well A, where (**a**) is the connected porosity φ^c , (**b**) is the effective porosity φ^e , (**c**) is the disconnected porosity φ^d , (**d**) is the microfracture-induced porosity φ^f , and (**e**) is the bound water content S_w^b .

sensitivity, %, m and n denote the component species and component sampling points, respectively, BI_{\min} denotes the minimum value of the brittleness index for each component, and V represents the content of each component. The MWS values from BI_1 to BI_5 are 15.87%, 18.20%, 22.21%, 13.34%, and 23.72%, respectively. From these results, we can preliminarily select the brittleness indexes BI_3 and BI_5 for Well A.

Second, studies have shown that porosity negatively affects rock brittleness in shale gas reservoirs (Walton et al., 2017). For BI_3 and BI_5 , we have analyzed the influence of the porosity from 1% to 10% on the brittleness index for different quartz contents (30%, 40%, and 50%), as shown in Fig. 7. In summary, BI_3 and BI_5 both increase as the quartz content increases, which is consistent with the conclusions of the preliminary analysis. For the same quartz content, BI_3 decreases instead with increasing porosity, which is unsuitable for the brittleness index. BI_5 shows greater sensitivity with increasing porosity, making it more suitable for the low-porosity shale of Well A.

Finally, we further analyze the effect of the organic matter content on the brittleness indexes in both the water-saturated and gas-saturated cases, as shown in Fig. 8. More importantly, BI_3 is

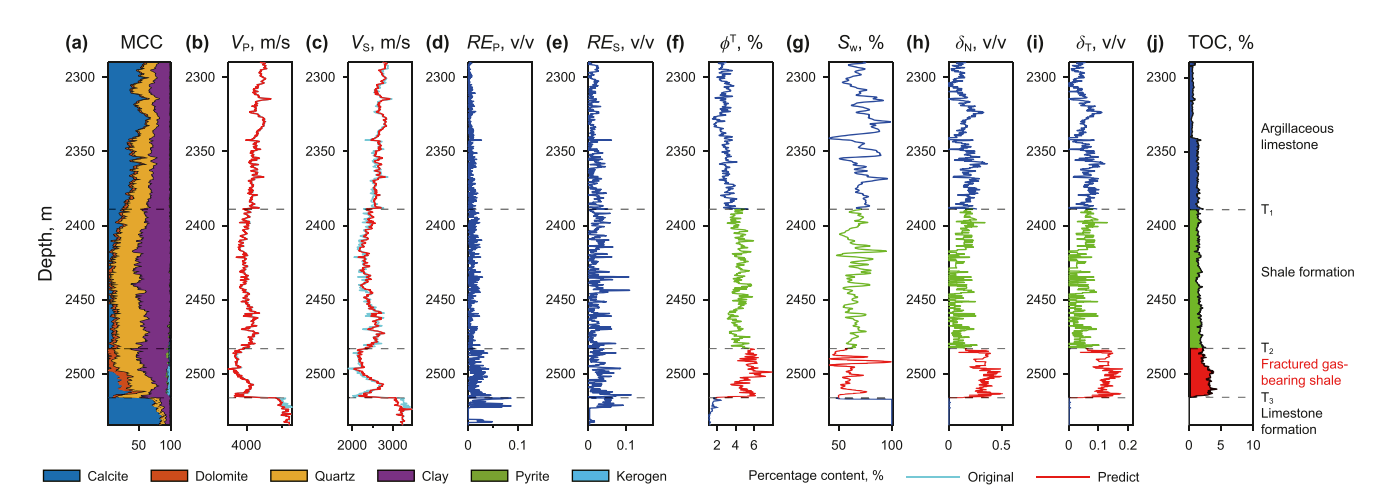


Fig. 4. Logging of Well A and modeling results from actual work areas in gas-bearing shale reservoirs, where (**a**) shows the rock mineral fraction and content MCC, (**b**) shows the P-wave velocity V_B , (**c**) shows the S-wave velocity V_S , (**d**) shows the relative error of the P-wave estimation RE_P , (**e**) shows the relative error of the S-wave estimation RE_S , (**f**) shows the porosity φ^T , (**g**) shows the water saturation S_w , (**h**) shows the predicted fracture normal weakness δ_N based on Fig. 3, (**i**) shows the predicted fracture tangential weakness δ_T based on Fig. 3, and (**j**) shows the TOC content.

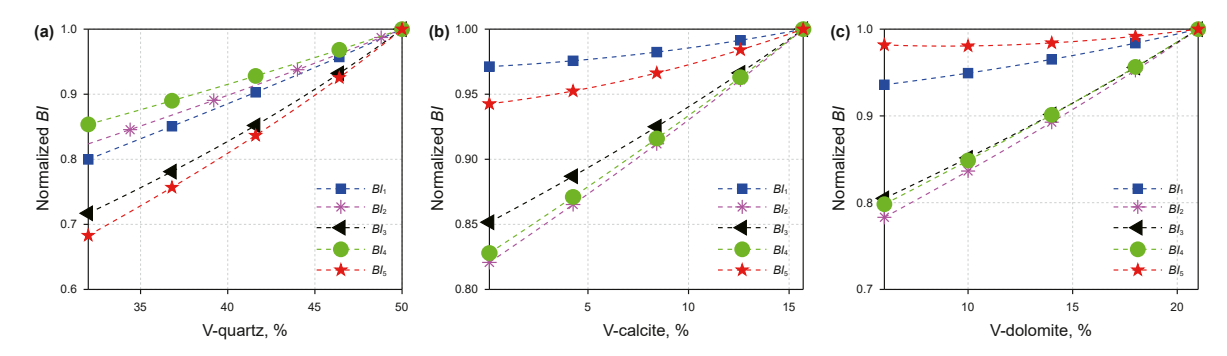


Fig. 6. Analysis of the contribution of different brittle mineral contents to the brittleness indexes, where (a) is quartz, (b) is calcite, and (c) is dolomite.

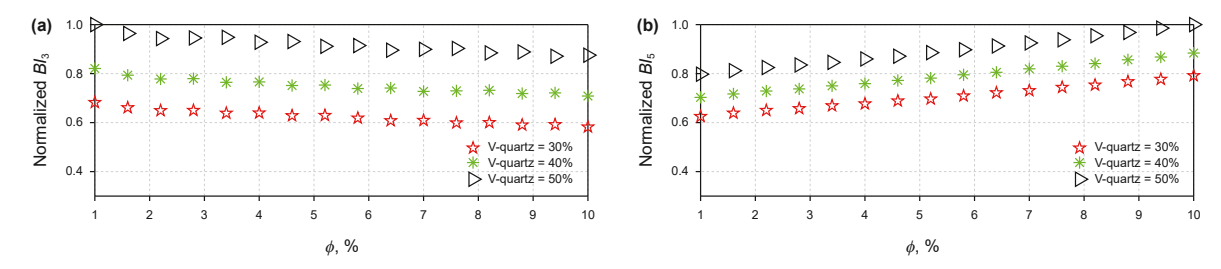


Fig. 7. Contributions of different quartz contents and porosities to brittleness indexes, where (a) is the contributions of brittleness index Bl_3 and (b) is the contributions of brittleness index Bl_5 .

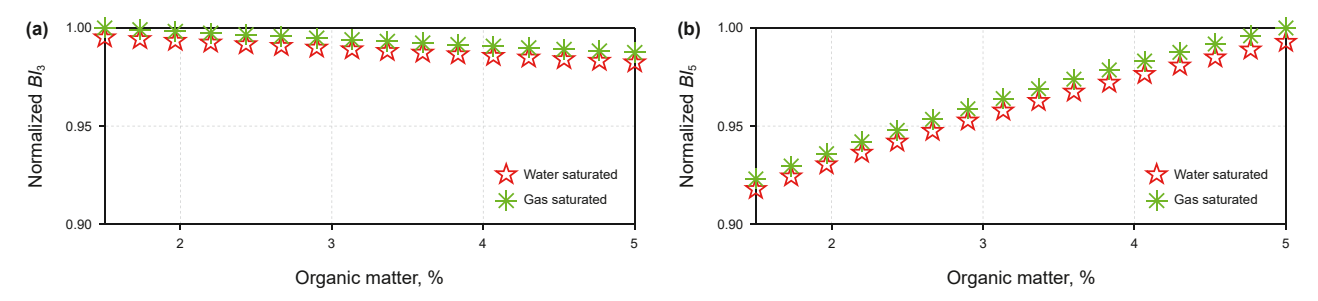


Fig. 8. Effect of organic matter content on brittleness index in different filling states, where (a) is the brittleness index BI₃ and (b) is the brittleness index BI₅.

negatively correlated with the organic matter content. In contrast, BI_5 is positively correlated with the content of organic matter content, which suggests that BI_5 is more sensitive in shale gas

reservoirs with high organic matter content and is generally positively correlated with TOC.

In conclusion, based on the petrophysical modeling of gas-

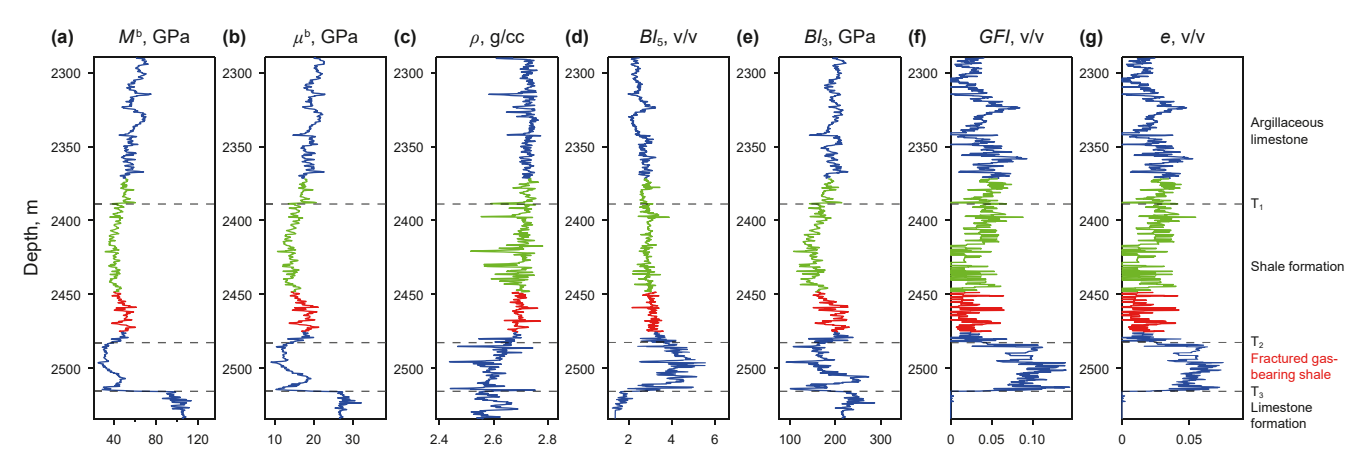


Fig. 9. Predicted well parameters based on petrophysical modeling in Fig. 3, where (**a**) is the P-wave modulus M^b , (**b**) is the S-wave modulus μ^b , (**c**) is the density ρ , (**d**) is the brittleness index Bl_5 , (**e**) is the brittleness index Bl_5 , (**e**) is the fracture gas indication factor *GFI*, and (**g**) is the fracture density e.

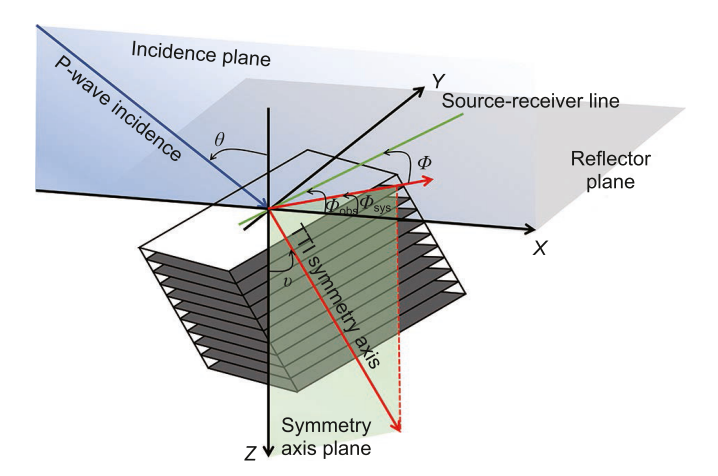


Fig. 10. Schematic diagram of P-wave incidence in the TTI medium (adapted from Pan et al., 2021).

bearing shale reservoirs, we comprehensively evaluated five widely acknowledged brittleness indexes for Well A. The most suitable brittleness index for characterizing the shale in this field area is BI_5 , which is influenced by the mineral fraction content, porosity, gas saturation, and organic matter content. Fig. 9 shows the related curves computed by using the logging data, for BI_3 in Fig. 9(e) and BI_5 in Fig. 9(d), and exhibits the P-wave modulus M^b , S-wave modulus μ^b , and density ρ for isotropic background parameter inversion, and the fracture gas indication factor GFI and fracture density e for anisotropic inversion. On Well A, BI_3 has high values in the argillaceous limestone of the upper section of the Longmaxi Formation above the well top T_1 , and in the limestone of the Baota Formation below the well top T_3 , and exhibits medium-high values in the shallow shale of the Longmaxi Formation from T_1 to T_2 , with

the lowest values in the high-quality fractured gas-bearing shale reservoirs from T_2 to T_3 , which is undesirable. In contrast, BI_5 has the highest values between T_2 and T_3 , as expected, which is where the target interval is.

The results of our brittleness index analysis demonstrate the reliability and validity of the brittleness index BI_5 ; however, this preferred brittleness index may only be suitable for the work area in the present study. Therefore, it is essential to evaluate location-specific conditions using the methodology outlined above.

2.3. Linearized PP-wave reflection coefficient in TTI media including the fracture parameters

To better characterize the seismic azimuthal anisotropy generated by subsurface tilted fractures, for an equivalent TTI medium subject to the assumption of weak anisotropy, the PP-wave reflection coefficient of the equivalent medium interface consists of two parts: an isotropic background term and an anisotropic perturbation term. For the isotropic term of the reflection coefficient, we utilize the $M-\mu-\rho$ formula (Zong et al., 2012) and anisotropic reflection coefficient equation that incorporates the perturbation of tilted fracture weaknesses (Pan et al., 2021; Qin et al., 2022; Huang et al., 2022), as shown in Fig. 10.

The expression for the linear PP-wave reflection coefficient in the TTI medium is given by

$$R_{\rm pp}^{\rm TTI}(\theta; \Phi, \nu) = R_{\rm pp}^{\rm iso}(\theta) + R_{\rm pp}^{\rm ani}(\theta; \Phi, \nu) \tag{13}$$

$$R_{\mathrm{PP}}^{\mathrm{iso}}(\theta) = k_{M^{\mathrm{b}}}(\theta) \frac{\Delta M^{\mathrm{b}}}{\overline{M}^{\mathrm{b}}} + k_{m^{\mathrm{b}}}(\theta) \frac{\Delta \mu^{\mathrm{b}}}{\overline{\mu}^{\mathrm{b}}} + k_{\rho}(\theta) \frac{\Delta \rho}{\overline{\rho}} \tag{14}$$

$$R_{\rm PP}^{\rm ani}(\theta;\Phi,\nu) = k_{\delta_{\rm N}}(\theta;\Phi,\nu)\Delta\delta_{\rm N} + k_{\delta_{\rm T}}(\theta;\Phi,\nu)\Delta\delta_{\rm T} \tag{15}$$

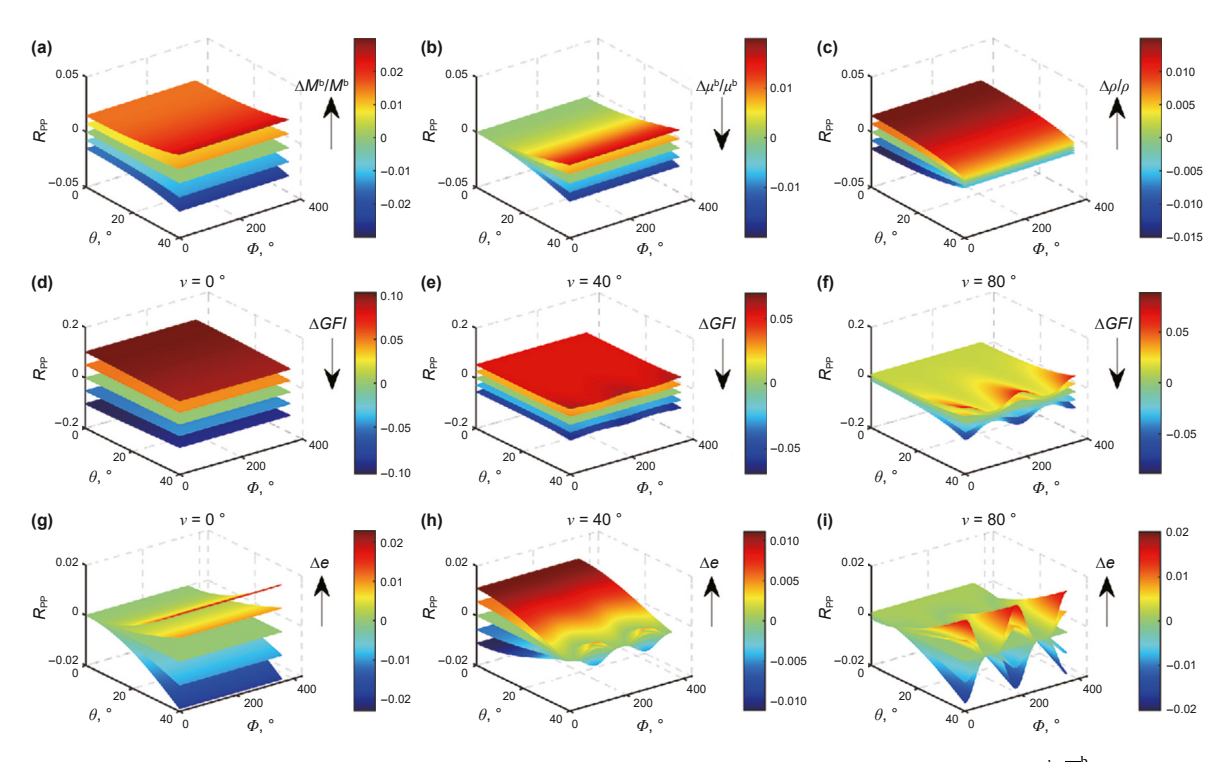


Fig. 11. Effect of different reflection coefficient terms on the PP-wave reflection coefficient, where (a) is the P-wave modulus reflectivity $\Delta M^b/\overline{M}^b$, (b) is the S-wave modulus reflectivity $\Delta \rho/\overline{\rho}$, (c) is the density reflectivity $\Delta \rho/\overline{\rho}$, (d)—(f) are the fracture gas indication factor reflectivity ΔGFI for different fracture inclinations, and (g)—(i) are the fracture density reflectivity Δe for different fracture inclinations of 0°, 40°, and 80°, respectively.

with

$$k_{M^{b}}(\theta) = \frac{\sec^{2}\theta}{4}, k_{\mu^{b}}(\theta) = -2g^{b}\sin^{2}\theta, k_{\rho}(\theta) = \left(\frac{1}{2} - \frac{\sec^{2}\theta}{4}\right) \tag{18}$$

$$(16a)$$

$$k_{\delta_{N}}(\theta;\Phi,v) = -\frac{\sec^{2}\theta}{4} \left\{ \begin{aligned} \cos^{4}\theta \left[\gamma^{b}\cos^{2}v \left(\sin^{4}\theta + 2\sin^{2}v \right) + \left(\sin^{2}v\sin^{4}\theta + \cos^{4}v + \left(\gamma^{b} \right)^{2}\sin^{4}v \right) \right] \\ + \gamma^{b}\sin^{4}\theta\sin^{2}\Phi \left(2\gamma^{b}\cos^{2}v\cos^{2}\Phi + 2\sin^{2}v\cos^{2}\Phi + \gamma^{b}\sin^{2}\Phi \right) \\ + \left[2\gamma^{b} \left(\gamma^{b}\sin^{2}v - 1 \right)\sin^{2}v + \left(\gamma^{b} - \frac{1}{2}\sin^{2}2v \right) \right]\sin^{2}\theta\cos^{2}\theta\cos^{2}\Phi \right] \end{aligned} \right\}$$

$$(16b)$$

$$k_{\text{GFI}}(\theta; \Phi, v) = \frac{4 \sec^{2} \theta}{3g^{b}(2g^{b} - 3)} \begin{cases} \cos^{4} \theta \left[\gamma^{b} \cos^{2} v \left(\sin^{4} \theta + 2 \sin^{2} v \right) + \left(\sin^{2} v \sin^{4} \theta + \cos^{4} v + \left(\gamma^{b} \right)^{2} \sin^{4} v \right) \right] \\ + \gamma^{b} \sin^{4} \theta \sin^{2} \Phi \left(2\gamma^{b} \cos^{2} v \cos^{2} \Phi + 2 \sin^{2} v \cos^{2} \Phi + \gamma^{b} \sin^{2} \Phi \right) \\ + \left[2\gamma^{b} \left(\gamma^{b} \sin^{2} v - 1 \right) \sin^{2} v + \left(\gamma^{b} - \frac{1}{2} \sin^{2} 2v \right) \right] \sin^{2} \theta \cos^{2} \theta \cos^{2} \Phi \right] \end{cases}$$

$$(19)$$

$$k_{e}(\theta; \Phi, v) = \frac{16}{3(3 - 2g^{b})} \begin{bmatrix} \left(\cos^{2} 2v + \cos^{2} v - \sin^{2} v \tan^{2} \theta \sin^{2} \Phi - \frac{1}{2}\sin^{2} 2v\right) g^{b} \sin^{2} \theta \cos^{2} \Phi \\ -\frac{1}{4}\sin^{2} 2v \left(\sin^{2} \theta \tan^{2} \theta \cos^{4} \Phi + \cos^{2} \theta\right) g^{b} \end{bmatrix}$$
(20)

$$\begin{split} k_{\delta_{\mathrm{T}}}(\theta;\Phi,\nu) &= \left(\cos^2 2\nu + \cos^2 \nu - \sin^2 \nu \tan^2 \theta \sin^2 \Phi\right. \\ &\left. - \frac{1}{2} \mathrm{sin}^2 \; 2\nu \right) g^{\mathrm{b}} \; \mathrm{sin}^2 \; \theta \cos^2 \Phi \\ &\left. - \frac{1}{4} \mathrm{sin}^2 \; 2\nu \left(\sin^2 \theta \tan^2 \theta \cos^4 \Phi + \cos^2 \theta\right) g^{\mathrm{b}} \right. \end{split} \tag{16c}$$

where θ denotes the incident angle of the P-wave; $\Phi(\Phi=\Phi_{\rm obs}-\Phi_{\rm sys})$ denotes the azimuthal angle between the normal orientation of the fractures ($\Phi_{\rm sys}$) and the observation line direction ($\Phi_{\rm obs}$); $\gamma^{\rm b}=1-2g^{\rm b}$; and v denotes the fracture tilt angle, which ranges from 0 to 90°.

From Eqs. (4) and (5), we can obtain the normal fracture weakness in terms of the fracture gas indication factor *GFI*:

$$\delta_{N} = \frac{16}{3g^{b}(3 - 2g^{b})}GFI \tag{17}$$

By substituting Eqs. (5) and (17) into Eq. (15), we can decouple the fracture gas indication factor *GFI* and fracture density e from the fracture perturbation. The anisotropic perturbation term of the PP-wave reflection coefficient can be simplified by combining the fracture density and fracture gas indication factor:

Eventually, the new linearized PP-wave reflection coefficient in the TTI medium can be derived simply as

$$R_{\rm pp}^{\rm TTI}(\theta; \Phi, v) = R_{\rm pp}^{\rm iso}(\theta) + New_{-}R_{\rm pp}^{\rm ani}(\theta; \Phi, v) \tag{21}$$

2.4. AVOAz inversion in TTI media with the sparsity constraints of the L_P quasinorm

To choose a more favorable inversion strategy, we need to examine the derived PP wave reflection coefficient for the TTI medium in Eq. (21) from the contribution of each reflectivity parameter, and the relationships among the parameters and the azimuthal angle, incident angle, and fracture inclination. Fig. 11 illustrates the impact of different reflection coefficient terms on the PP-wave reflection coefficient. The direction of the arrows shows an increase in the parameters, and all the reflectivity parameters vary from -0.06 to 0.06 at an interval of 0.03. We can conclude that the P-wave modulus reflectivity $\Delta M^b/\overline{M}^b$ contributes essentially over the entire range of incident angles in Fig. 11(a), which facilitates its seismic inversion. The S-wave modulus reflectivity $\Delta \mu^b/\overline{\mu}^b$ contributes more and responds more sensitively at larger incident angles or offsets in Fig. 11(b), indicating that seismic data at larger incident angles are more beneficial for its inversion. The density

reflectivity $\Delta \rho/\bar{\rho}$ in Fig. 11(c) is more sensitive at smaller incident angles. Nevertheless, these three parameters above are all independent of the azimuthal angle, which can be inverted via the prestacked isotropic inversion to predict the optimum brittleness index BI_5 for the work area. Second, the fracture gas indication factor reflectivity ΔGFI in Fig. 11(e) and (f) and the fracture density reflectivity Δe in Fig. 11(h) and (i) show periodic variations with the azimuthal angle, which requires the anisotropic seismic inversion. Moreover, when the fracture inclination decreases to 0°, the TTI medium degenerates to a vertical transversely isotropic (VTI) medium without azimuthal anisotropy, and the anisotropic strength increases with increasing inclination angle, indicating the necessity of considering the fracture inclination angle.

With the weak anisotropy, it is necessary to introduce the azimuthal differences to eliminate the isotropic background component and reduce the number of one-time inversion parameters, which helps to improve the stability and accuracy of the anisotropic parameter inversion. Based on the above analysis of the contribution of each parameter to the PP-wave reflection coefficient, we optimize the two-step inversion strategy to invert the isotropic elastic parameters and anisotropic fracture parameters. First, azimuthal amplitude difference seismic data between two orthogonal azimuths ($\Phi_1=0^\circ$ and $\Phi_2=\pi/2$) are exploited to eliminate the isotropic background component so that we can obtain the anisotropic perturbation of the PP-wave reflection coefficient as follows:

$$\Delta R_{\text{PP}}^{\text{TTI}}(\theta; v) = \Delta k_{\text{GFI}}(\theta; v) \Delta GFI + \Delta k_{\text{e}}(\theta; v) \Delta e$$
 (22)

$$\Delta k_{\text{GFI}}(\theta; v) = k_{\text{GFI}}(\theta; \Phi = \pi/2, v) - k_{\text{GFI}}(\theta; \Phi = 0^{\circ}, v)$$
 (23)

$$\Delta k_{\rm e}(\theta; v) = k_{\rm e}(\theta; \Phi = \pi/2, v) - k_{\rm e}(\theta; \Phi = 0^{\circ}, v) \tag{24}$$

where ΔR_{PP}^{TTI} denotes the PP-wave reflection coefficient of the anisotropic perturbation part.

To utilize seismic data to invert relevant fracture parameters, it is assumed that the seismic data are synthesized by the forward operator $G^{\rm ani}$ and anisotropic perturbation reflection coefficient $\Delta R^{\rm ani}_{\rm PP}$ and that the number of vertical samplings is N.

$$\Delta \mathbf{S} = \mathbf{G}^{\text{ani}} \Delta \mathbf{R}_{\text{pp}}^{\text{ani}} = \mathbf{W} \mathbf{B} \mathbf{D} \mathbf{X} \tag{25}$$

with

$$\Delta \mathbf{S} = \begin{bmatrix} s_{\text{PP}}(\theta_1, \Phi_2) - s_{\text{PP}}(\theta_1, \Phi_1) \\ s_{\text{PP}}(\theta_2, \Phi_2) - s_{\text{PP}}(\theta_2, \Phi_1) \\ \vdots \\ s_{\text{PP}}(\theta_M, \Phi_2) - s_{\text{PP}}(\theta_M, \Phi_1) \end{bmatrix}_{MN \times 1}$$
(26)

$$\mathbf{W}_{0} = \begin{bmatrix} w_{1} & 0 & \cdots & 0 \\ \vdots & w_{1} & \ddots & \vdots \\ w_{sc} & \vdots & \ddots & 0 \\ 0 & w_{sc} & \cdots & w_{1} \\ \vdots & \ddots & \ddots & \vdots \\ 0 & \cdots & 0 & w_{sc} \end{bmatrix}_{(N-1)\times 1}$$
(27)

$$\mathbf{W} = diag[\mathbf{W}_0 \quad \mathbf{W}_0 \cdots \mathbf{W}_0]_{M(N-1) \times M(N-1)}$$
(28)

$$\boldsymbol{B} = \begin{bmatrix} \boldsymbol{F}(\theta_1) & \boldsymbol{U}(\theta_1) \\ \boldsymbol{F}(\theta_2) & \boldsymbol{U}(\theta_2) \\ \vdots & \vdots \\ \boldsymbol{F}(\theta_M) & \boldsymbol{U}(\theta_M) \end{bmatrix}_{M(N-1) \times 2(N-1)}$$
(29)

$$\mathbf{F}(\theta_i; v) = \operatorname{diag}[\Delta k_{\mathrm{GFI}}(\theta_i; v) \quad \Delta k_{\mathrm{GFI}}(\theta_i; v) \cdots \Delta k_{\mathrm{GFI}}(\theta_i; v)]_{(N-1) \times (N-1)}$$
(30)

$$\label{eq:update} \begin{split} \boldsymbol{U}(\theta_i; \boldsymbol{v}) &= \text{diag}[\Delta k_{\text{e}}(\theta_i; \boldsymbol{v}) \quad \Delta k_{\text{e}}(\theta_i; \boldsymbol{v}) \cdots \Delta k_{\text{e}}(\theta_i; \boldsymbol{v})\,]_{(N-1) \times (N-1)} \end{split} \tag{31}$$

$$\mathbf{D} = \operatorname{diag}[\mathbf{D}_0 \quad \mathbf{D}_0]_{2(N-1) \times 2N} \tag{32}$$

$$\mathbf{D}_{0} = \begin{bmatrix} -1 & 1 & 0 & \cdots & 0 \\ 0 & -1 & 1 & \ddots & \vdots \\ \vdots & \ddots & \ddots & \ddots & 0 \\ 0 & \cdots & \cdots & -1 & 1 \end{bmatrix}_{(N-1)\times N}$$
(33)

$$\mathbf{X} = [\mathbf{GFI} \ \mathbf{e}]_{2N \times 1}^{\mathrm{T}} \tag{34}$$

$$\mathbf{GFI} = [GFI_1 \quad GFI_2 \quad \cdots \quad GFI_N]_{N \times 1}^{T}$$
(35)

$$\mathbf{e} = \begin{bmatrix} e_1 & e_2 & \cdots & e_N \end{bmatrix}_{N \times 1}^{\mathrm{T}} \tag{36}$$

where \boldsymbol{X} denotes the inversion parameter matrix, \boldsymbol{M} is the number of incident angles, the superscript T represents the transposition of the matrix, $\Delta \boldsymbol{S}$ denotes the azimuth amplitude difference seismic data, \boldsymbol{W} denotes the wavelet matrix of the incident angles and azimuthal angles, \boldsymbol{B} is the coefficient matrix, the subscript sc denotes the length of the wavelet, and the symbol diag represents the diagonal matrix.

We use both the low-frequency constraint term and the L_P quasinorm sparsity constraint term to construct the objective inversion function:

$$J(\pmb{X}) = \underset{\pmb{X}}{\operatorname{argmin}} \left\{ \| \pmb{W} \pmb{B} \pmb{D} \pmb{X} - \Delta \pmb{S} \|_{2}^{2} + \omega \| \pmb{X} - \pmb{X}_{0} \|_{2}^{2} + \alpha \| \pmb{B} \pmb{D} \pmb{X} \|_{p}^{p} \right\}$$
(37)

where $\| \|_2^2$ and $\| \|_p^p$ specify the L_2 norm and L_P quasinorm $[p \in (0,1)]$, respectively; $\textbf{\textit{X}}_0$ denotes the initial model obtained by interpolation extrapolation of $\textbf{\textit{X}}$, followed by Gaussian low-pass filtering; ω is the coefficient of the initial model constraint term; and α is the coefficient for the sparsity constraint. We introduce the alternating direction method of multipliers (ADMM) algorithm to solve the nonlinear problem in Eq. (37), and the Lagrangian multiplier $\textbf{\textit{H}} = \textbf{\textit{BDX}}$ and dual term $\textbf{\textit{Q}}$ transform the optimization problem into a linear problem:

$$J(\boldsymbol{X}, \boldsymbol{H}, \boldsymbol{Q}) = \underset{\boldsymbol{X}, \boldsymbol{H}, \boldsymbol{Q}}{\operatorname{argmin}} \Big\{ \|\boldsymbol{W}\boldsymbol{B}\boldsymbol{D}\boldsymbol{X} - \Delta\boldsymbol{S}\|_{2}^{2} + \omega \|\boldsymbol{X} - \boldsymbol{X}_{0}\|_{2}^{2} + \alpha \|\boldsymbol{H}\|_{p}^{p} \\ + \beta \|\boldsymbol{H} - \boldsymbol{B}\boldsymbol{D}\boldsymbol{X} - \boldsymbol{Q}\|_{2}^{2} \Big\}$$
(38)

where β denotes the correlation between the Lagrange multiplier and dual terms. The linear problem in Eq. (38) is transformed into subobjective functions for X, H, and Q and the iterative update expressions are obtained after solving by ADMM, respectively, in that order:

Table 3 Inversion workflow based on the ADMM of the L_P quasinorm.

Algorithm: Inversion of prestack seismic parameters based on the ADMM and iterative shrinkage thresholding algorithm (ISTA)

Input: ΔS , X_0 , B, D, W, λ , α , β , p, maximum error threshold ε . Initial parameters: k=0, $X^{(0)}=X_0$, $H^{(0)}=0$, $Q^{(0)}=0$.

1 Iteratively updated $X^{(k+1)}$ by Eq. (39).

2 Iteratively updated $H^{(k+1)}$ by Eqs. (40) and (41).

3 Iteratively updated $Q^{(k+1)}$ by Eq. (42).

4 Termination conditions: If $\frac{\left\|X^{(k+1)}-X^{(k)}\right\|_2}{\left\|X^{(k)}\right\|_2} \leq \varepsilon$, iteration of updates ceased.

Otherwise, k=k+1, repeat the steps 1-4.

5 Obtain the parameters matrix $X^{(k+1)}$.

Optimal inversion results: fracture gas indication factor GFI and fracture density e

$$\mathbf{X}^{(k+1)} = \left\{ (\mathbf{W}\mathbf{B}\mathbf{D})^{\mathrm{T}}\mathbf{W}\mathbf{B}\mathbf{D} + \omega\mathbf{I} + \beta \left[(\mathbf{B}\mathbf{D})^{\mathrm{T}}\mathbf{B}\mathbf{D} \right] \right\}^{-1} \\ \cdot \left\{ (\mathbf{W}\mathbf{B}\mathbf{D})^{\mathrm{T}}\Delta\mathbf{S} + \omega\mathbf{X}_{0} + \beta (\mathbf{B}\mathbf{D})^{\mathrm{T}} \left[\mathbf{H}^{(k)} - \mathbf{Q}^{(k)} \right] \right\}$$
(39)

where I denotes a unit matrix of the same dimension as the matrix D^TD , and k is the iterative number.

$$\mathbf{H}^{(k+1)} = \operatorname{sign}\left[\mathbf{BDX}^{(k+1)} + \mathbf{Q}^{(k)}\right] \cdot \max\left[\left|\mathbf{BDX}^{(k+1)} + \mathbf{Q}^{(k)}\right| - \left(\frac{\beta}{\alpha}\right)^{p-2}\left|\mathbf{BDX}^{(k+1)} + \mathbf{Q}^{(k)}\right|^{p-1}, 0\right]$$

$$(40)$$

where $sign(\zeta)$ is a symbolic function defined as Eq. (41)

$$sign(\zeta) = \begin{cases} 1 & , \zeta > 0 \\ 0 & , \zeta = 0 \\ -1 & , \zeta < 0 \end{cases}$$
 (41)

$$\mathbf{Q}^{(k+1)} = \mathbf{Q}^{(k)} + \left[\mathbf{BDX}^{(k+1)} - \mathbf{H}^{(k+1)} \right]$$
 (42)

In Table 3, we summarized the inversion framework of the

fracture density e and fracture gas indication factor GFI based on the L_P quasinorm.

After obtaining the inversion results of the anisotropic parameters in the first step, the remaining seismic amplitude data are used in the second step to invert the isotropic background parameters in Eq. (14), including the isotropic parameters M^b , μ^b , and ρ , using the same inversion algorithm in Table 3. Seismic data that eliminate the effects of fractures are obtained:

$$\mathbf{S}^{\mathrm{iso}} = \mathbf{S} - \mathbf{W}\mathbf{M}'\mathbf{D}\mathbf{X} = \mathbf{W}\mathbf{B}^{\mathrm{iso}}\mathbf{X}^{\mathrm{iso}} \tag{43}$$

with

$$\tilde{\boldsymbol{B}} = \begin{bmatrix} \boldsymbol{F}(\theta_1, \Phi_i) & \boldsymbol{U}(\theta_1, \Phi_i) \\ \boldsymbol{F}(\theta_2, \Phi_i) & \boldsymbol{U}(\theta_2, \Phi_i) \\ \vdots & \vdots \\ \boldsymbol{F}(\theta_M, \Phi_i) & \boldsymbol{U}(\theta_M, \Phi_i) \end{bmatrix}_{M(N-1) \times 2(N-1)}$$

$$(44)$$

$$\boldsymbol{B}^{\text{iso}} = \begin{bmatrix} \boldsymbol{C}(\theta_1) & \boldsymbol{V}(\theta_1) & \boldsymbol{Y}(\theta_1) \\ \boldsymbol{C}(\theta_2) & \boldsymbol{V}(\theta_2) & \boldsymbol{Y}(\theta_2) \\ \vdots & \vdots & \vdots \\ \boldsymbol{C}(\theta_M) & \boldsymbol{V}(\theta_M) & \boldsymbol{Y}(\theta_M) \end{bmatrix}_{M(N-1)\times 3(N-1)}$$
(45)

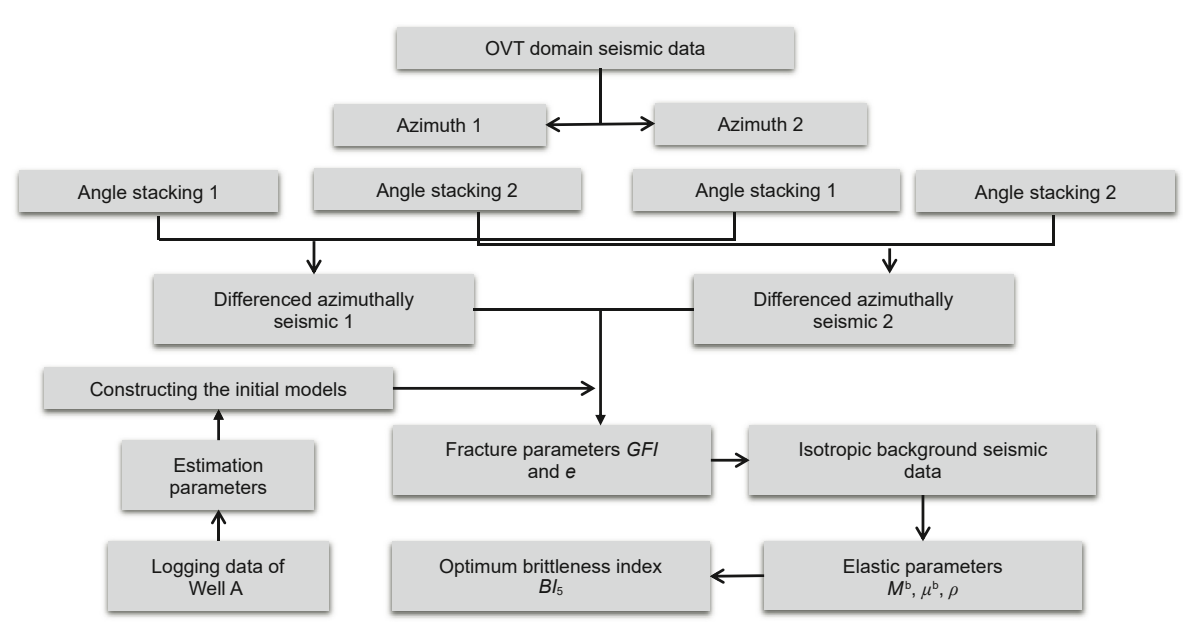


Fig. 12. Workflow of the inversion strategy.

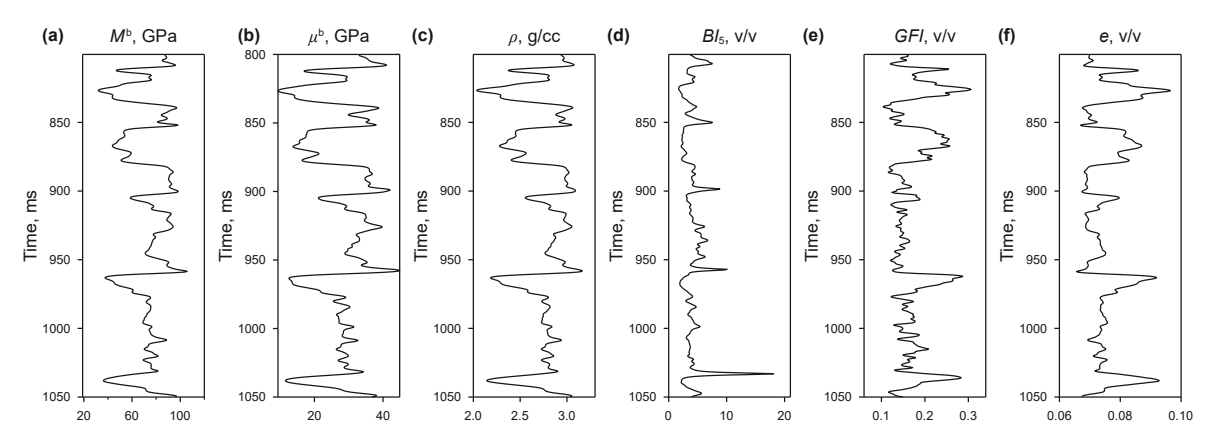


Fig. 13. Well curves used for model testing, where (**a**) is the P-wave modulus M^b , (**b**) is the S-wave modulus μ^b , (**c**) is the density ρ , (**d**) is the brittleness index Bl_5 , (**e**) is the fracture gas indication factor GFI and (**f**) is the fracture density e.

$$\mathbf{C}(\theta_i) = \operatorname{diag} \begin{bmatrix} k_{M^b}(\theta_i) & k_{M^b}(\theta_i) \cdots k_{M^b}(\theta_i) \end{bmatrix}_{(N-1) \times (N-1)}$$

$$\mathbf{Y}(\theta_i) = \operatorname{diag} [k_{\rho}(\theta_i) & k_{\rho}(\theta_i) \cdots k_{\rho}(\theta_i)]_{(N-1) \times (N-1)}$$

$$(48)$$

$$\mathbf{V}(\theta_i) = \operatorname{diag}\left[k_{\mu^b}(\theta_i) \quad k_{\mu^b}(\theta_i) \cdots k_{\mu^b}(\theta_i)\right]_{(N-1)\times(N-1)} \tag{47} \qquad \mathbf{X}^{\operatorname{iso}} = \left[\frac{\Delta \mathbf{M}^b}{\overline{\mathbf{M}}^b} \quad \frac{\Delta \mu^b}{\overline{\mu}^b} \quad \frac{\Delta \rho}{\overline{\rho}}\right]_{3N\times 1}^{1}$$

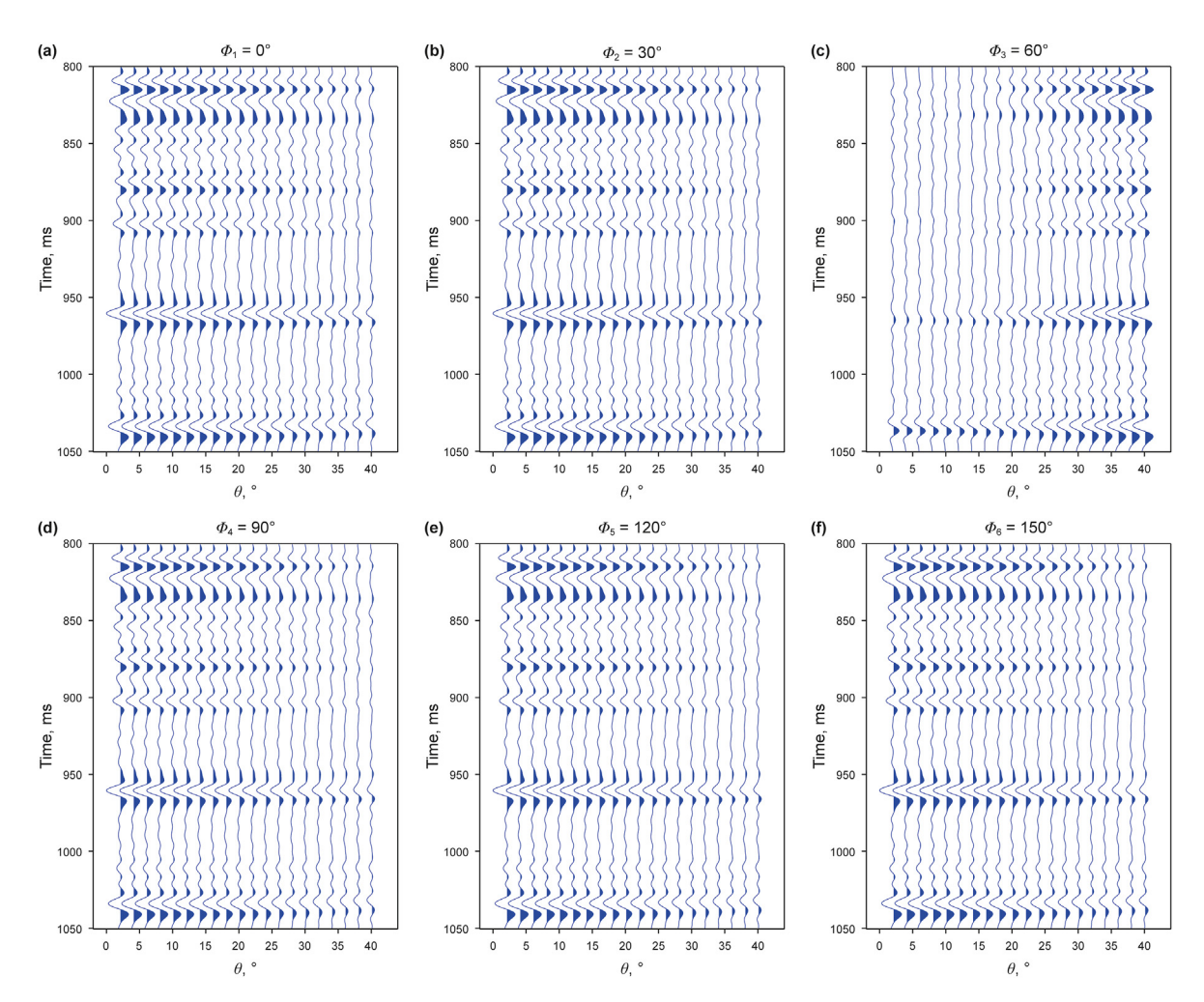


Fig. 14. Synthesized noiseless azimuthal seismic data with (a) an azimuth of 0° , (b) an azimuth of 30° , (c) an azimuth of 60° , (d) an azimuth of 90° , (e) an azimuth of 120° , and (f) an azimuth of 150° .

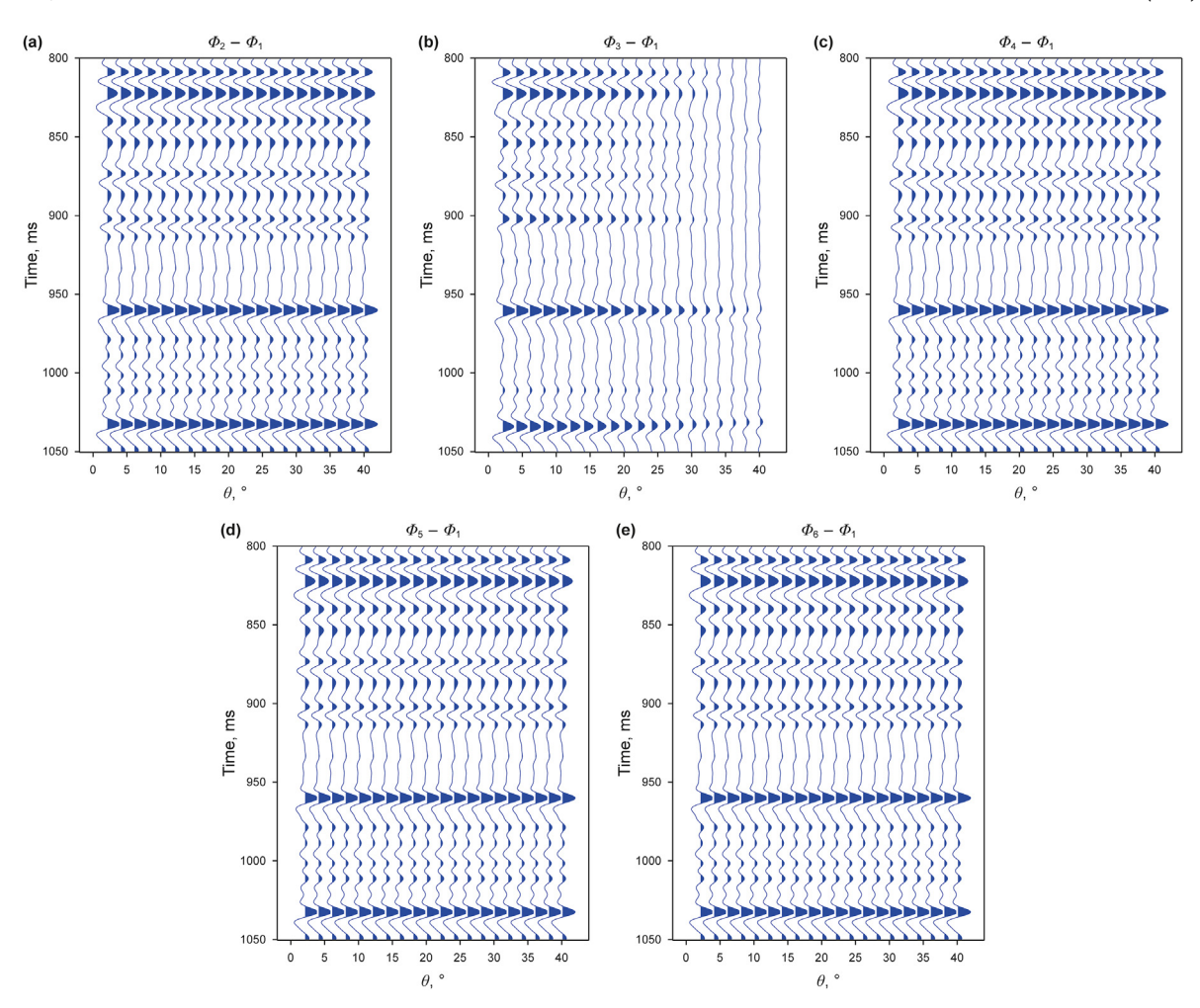


Fig. 15. Noise-free synthetic azimuthal difference seismic data with (a) $\Phi_2 - \Phi_1$, (b) $\Phi_3 - \Phi_1$, (c) $\Phi_4 - \Phi_1$, (d) $\Phi_5 - \Phi_1$, and (e) $\Phi_6 - \Phi_1$, respectively.

where \mathbf{S} denotes the azimuthal seismic data, $\mathbf{S}^{\mathrm{iso}}$ indicates the residual seismic amplitude data, representing the isotropic part, and $\mathbf{X}^{\mathrm{iso}}$ is a parameter matrix of the P-wave modulus, S-wave modulus, and density not associated with azimuths or fracture dips. Finally, we have summarized the workflow of this paper's parameter inversion strategy in Fig. 12.

3. Model testing and field-data application

3.1. Synthetic data

To validate the effectiveness and robustness of the stepwise inversion algorithm proposed in Section 2.4, we design a TTI model with a fracture tilt angle of 70°. We first calculated the elastic and fracture parameters on the well of this model, which are presented in Fig. 13. The isotropic elastic parameters are the P-wave modulus M^b , S-wave modulus μ^b , and density ρ ; the anisotropic parameters are the fracture gas indication factor *GFI* and fracture density e; and the brittleness index BI_5 is calculated indirectly with Eq. (11) based on the isotropic elastic parameters. Using the Richer wavelet with a main frequency f_0 of 30 Hz in Eq. (50), we convolutionally synthesize azimuthal seismic data with different signal-to-noise ratios (SNRs) according to Eq. (21), which mainly includes the six azimuthal angles of 0° , 30° , 60° , 90° , 120° , and 150° , sequentially.

Fig. 14 shows the synthesized noiseless azimuthal seismic data, with incident angles ranging from 0 to 40° for each azimuth at an

interval of 2°. To eliminate the isotropic background of synthetic seismic data, the synthetic seismic data with different azimuthal angles were differenced and employed to invert the anisotropic fracture parameters, namely the fracture gas indication factor *GFI* and the fracture density *e*. The five sets of azimuthally differenced synthetic seismic data containing noiseless data are displayed in Fig. 15.

$$w(t) = \left[1 - 2(\pi f_0 t)^2\right] e^{\left[-(\pi f_0 t)^2\right]}$$
 (50)

where f_0 denotes the main frequency of the Richer wavelet.

To verify the noise resistance of the inversion algorithm in this article, we attach a certain degree of random noise to the synthetic seismic data recorded at different azimuthal angles, as shown in Fig. 16, and simultaneously, we generate the relevant azimuthal difference seismic synthetic data, as shown in Fig. 17.

Fig. 18 illustrates the noiseless parameter inversion results obtained using the azimuthal seismic data in Fig. 14 and the amplitude difference seismic data in Fig. 15; the red curves represent the inversion results, the black curves represent the well data, and blue curves represent the initial model. The inversion results show that the couplings between the inversion results in red and the modeled data in black are strong. The isotropic parameters can be satisfactorily inverted, and the weakly anisotropic fracture parameters can also be obtained with high accuracy due to the advantage of the separate inversion in the approach presented in this paper. Notably,

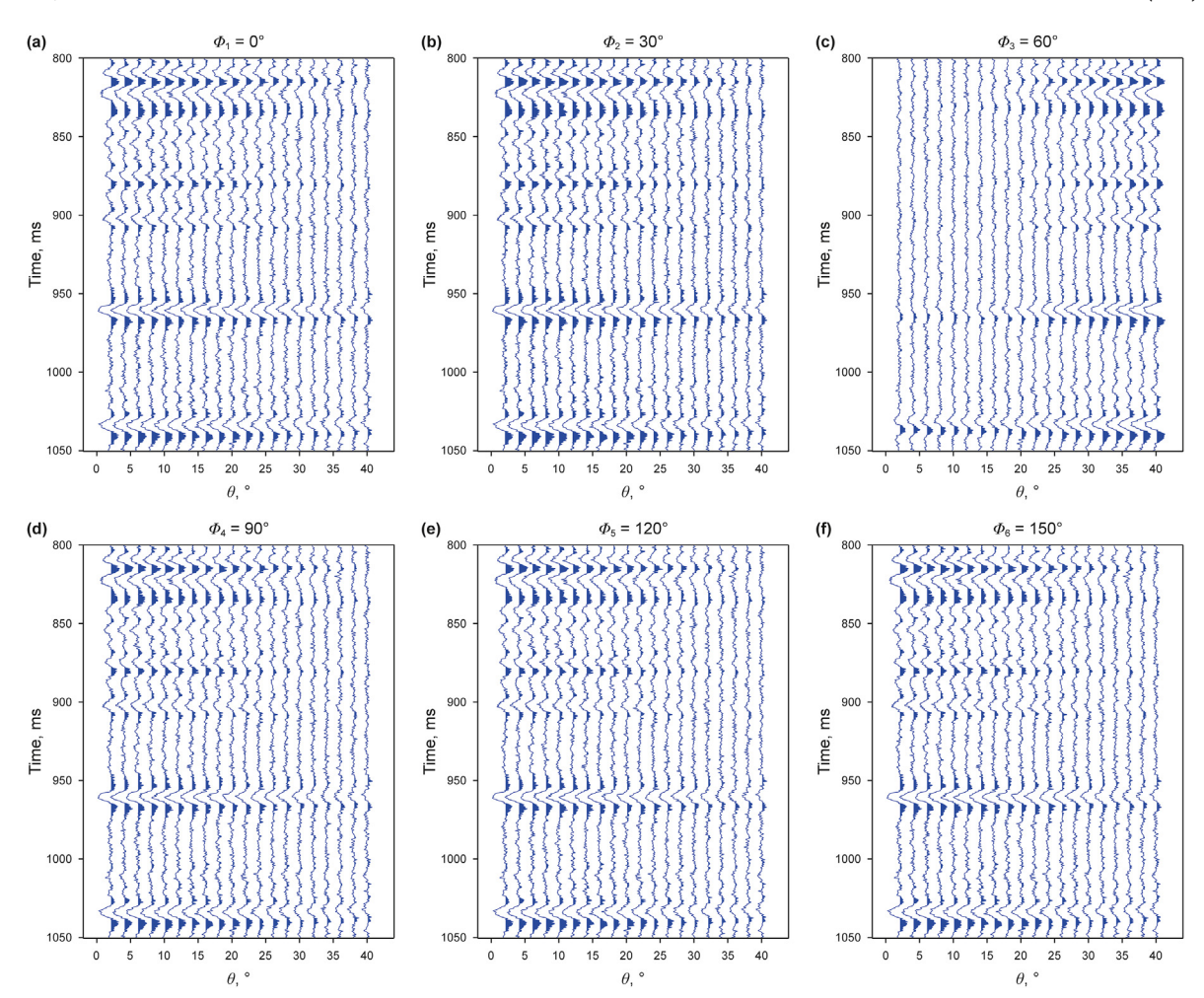


Fig. 16. Synthesized azimuthal seismic data for SNR = 5 with (a) an azimuth of 0° , (b) an azimuth of 30° , (c) an azimuth of 60° , (d) an azimuth of 90° , (e) an azimuth of 90° , and (f) an azimuth of 90° , (e) an azimuth of 90

the brittleness indices calculated indirectly from the inversion results of the isotropic parameters agree very well with the logging data. Fig. 19 illustrates the robustness test results of the inversion algorithm, using the noise-added azimuthal seismic data in Fig. 16 and the amplitude difference seismic data in Fig. 17. The inversion results are undeniably corrupted by random noise. However, the relative trend of the inversion results is still reasonable and acceptable, indicating that the inversion algorithm has satisfactory robustness.

To quantitatively analyze the effectiveness and robustness of the inversion algorithm, we introduce the correlation coefficient in Eq. (51) to calculate the coupling between the inversion result and the model curve for each parameter, which characterizes the degree of correlation between the two vectors, and in general.

$$cc = \frac{\sum_{i} (\kappa_{i} - \overline{\kappa})(\xi_{i} - \overline{\xi})}{\sqrt{\sum_{i} (\kappa_{i} - \overline{\kappa})^{2} \sum_{i} (\xi_{i} - \overline{\xi})^{2}}}$$
(51)

where κ and ξ represent the inversion result vector and the actual model vector, respectively; the overline indicates the average value, and the closer the absolute value of cc is to 1, the greater the correlation.

Fig. 20 illustrates a histogram of the error statistics relative to the modeled data for the noiseless inversion results of Fig. 18. This intuitively demonstrates that the relative errors of all the parameters are mainly low. The correlation coefficients of the predicted parameters are all greater than 0.998 in this case, indicating that the inversion accuracy in the noiseless case is relatively high. Moreover, Fig. 21 exhibits that the relative errors of the inversion results in the case of noise disturbance are greater than those in the noiseless case. In the case of noise disturbance, the correlation coefficients of all directly predicted parameters are greater than 0.92, and the indirectly calculated brittleness index is greater than 0.82 in the case of noise disturbance. The relative errors of the parameters are still within the acceptable range, and the calculated brittleness index is relatively reasonable. In summary, the synthetic data tests in this article show that the inversion strategy based on the L_P quasinorm theory possesses a certain degree of effectiveness and noise resistance and can be applied in practice.

3.2. Field-data application

To verify the effectiveness of this method in predicting the fracture development, fracture gas content, and the shale brittleness distribution in fractured gas-bearing shale reservoirs, a specific area of the Sichuan Basin, China, as shown in Fig. 22, is adopted for further analysis. Fig. 4 exhibits the logging data and fracture weakness prediction results of Well A. The section from T₂ to T₃ at Well A is a fractured, high-quality, gas-bearing shale reservoir with vertical depths of 2483 m—2516 m, which is the central reservoir

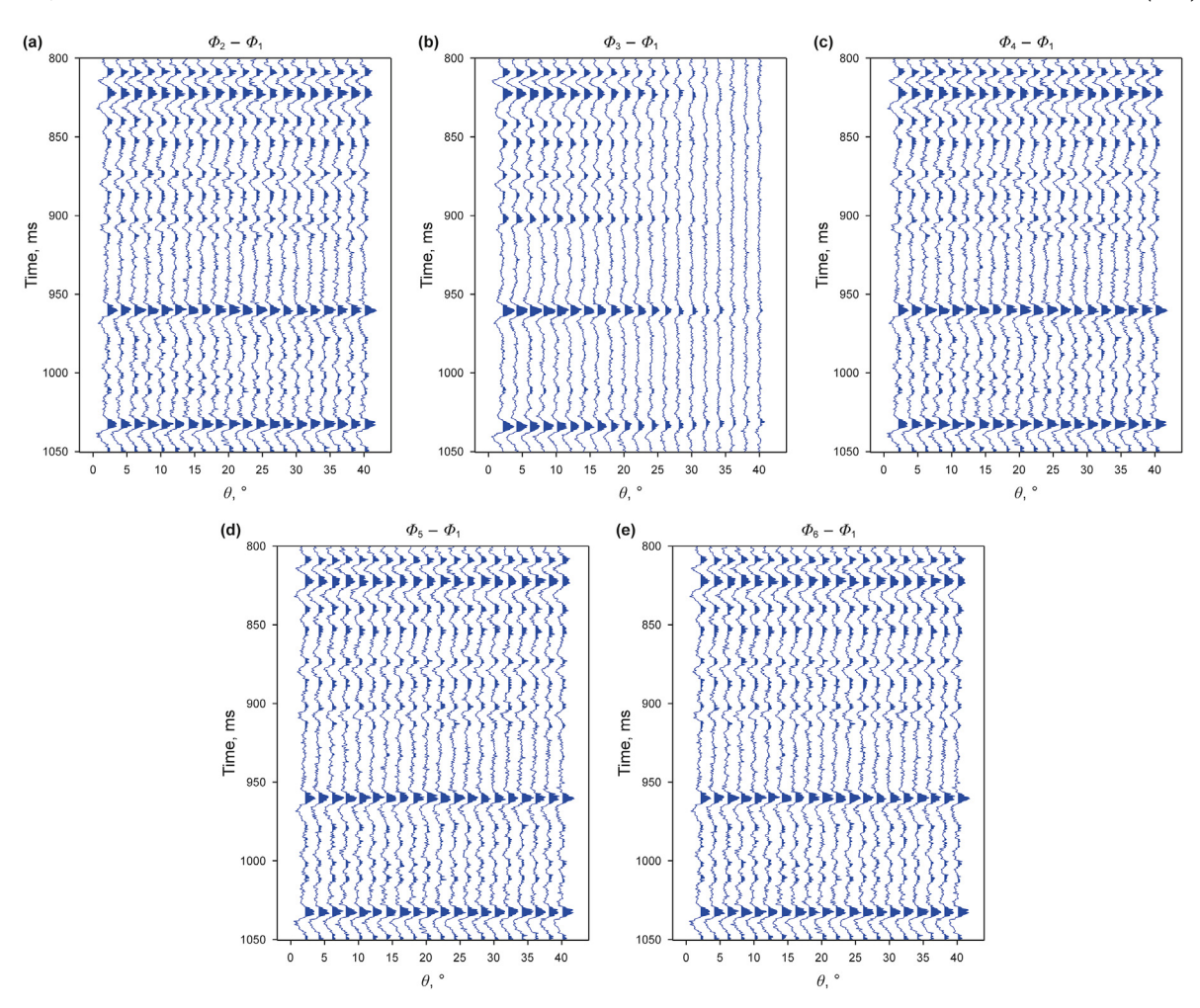


Fig. 17. Synthetic azimuthal difference seismic data for SNR = 5 with (a) $\Phi_2 - \Phi_1$, (b) $\Phi_3 - \Phi_1$, (c) $\Phi_4 - \Phi_1$, (d) $\Phi_5 - \Phi_1$, and (e) $\Phi_6 - \Phi_1$, respectively.

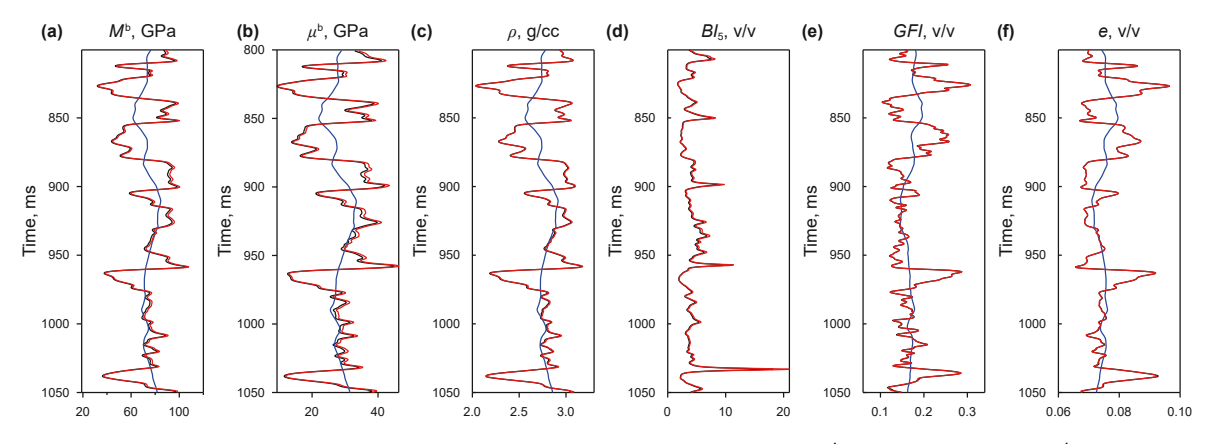


Fig. 18. Comparison between the actual values and the inversion results (no noise), where (a) is the P-wave modulus M^b , (b) is the S-wave modulus μ^b , (c) is the density ρ , (d) is the brittleness index Bl_5 , (e) is the fracture gas indication factor GFI and (f) is the fracture density ρ , with the red curves representing the inversion results, the black curves representing the modeled well data, and the blue curves representing the initial model.

location for such prediction work due to its high porosity, high values of fracture weaknesses indicating fracture development, and high TOC content indicating the high hydrocarbon production capacity of this section of shale. Fig. 9 presents the main parameters prepared for prestack seismic inversion, with a high brittleness index BI_5 in the destination section, and high values of the predicted fracture density and fracture gas indication factor are

exhibited. Before commencing the reservoir inversion prediction, the azimuth of fracture development (fracture strike) and fracture dip are determined from the fullbore formation microimager (FMI) image interpretation results in Fig. 23. The fracture orientation is northeast to southwest, and the fracture dip angle is mainly concentrated at 70° . Then, the predictions of the reservoir geological sweet spot (*GFI*) and engineering sweet spots (*BI*₅ and *e*)

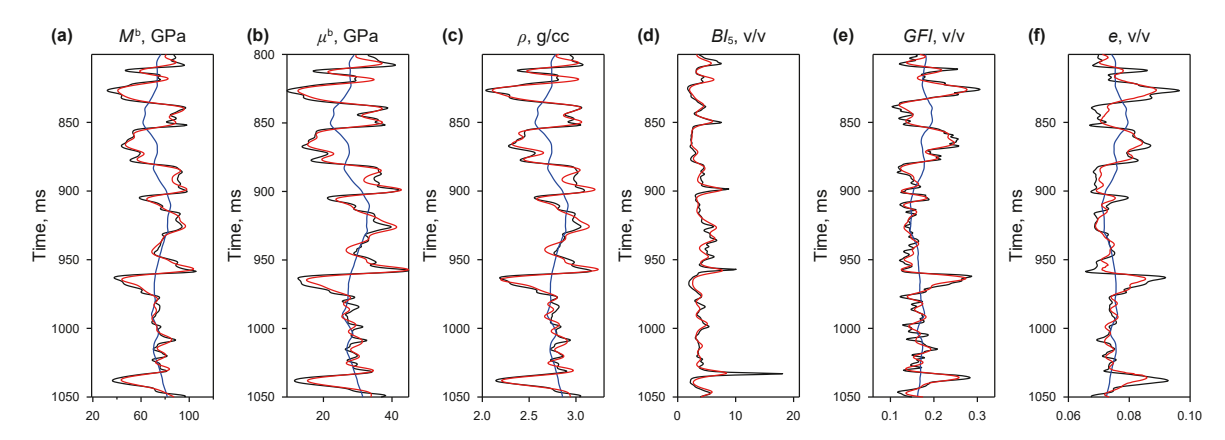


Fig. 19. Comparison between the actual values and the inversion results (SNR = 5), where (**a**) is the P-wave modulus M^b , (**b**) is the S-wave modulus μ^b , (**c**) is the density ρ , (**d**) is the brittleness index Bl_5 , (**e**) is the fracture gas indication factor GFl and (**f**) is the fracture density ρ , with the red curves representing the inversion results, the black curves representing the modeled well data, and the blue curves representing the initial model.

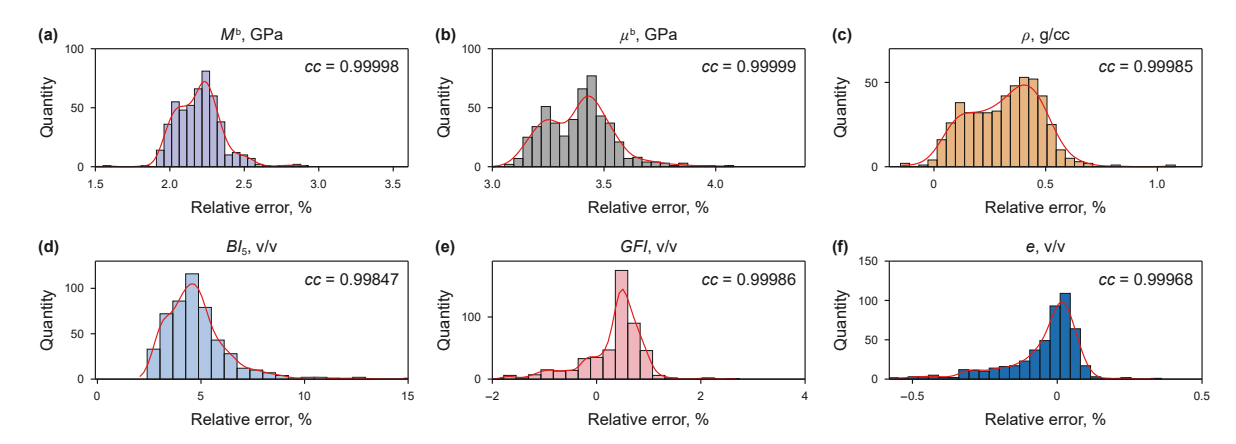


Fig. 20. Histogram of the relative error statistics of the noiseless inversion results in Fig. 18, where (**a**) is the P-wave modulus M^b , (**b**) is the S-wave modulus μ^b , (**c**) is the density ρ , (**d**) is the brittleness index BI_5 , (**e**) is the fracture gas indication factor GFI and (**f**) is the fracture density e, with cc denoting the correlation coefficient and the red line denoting the density fitting curve.

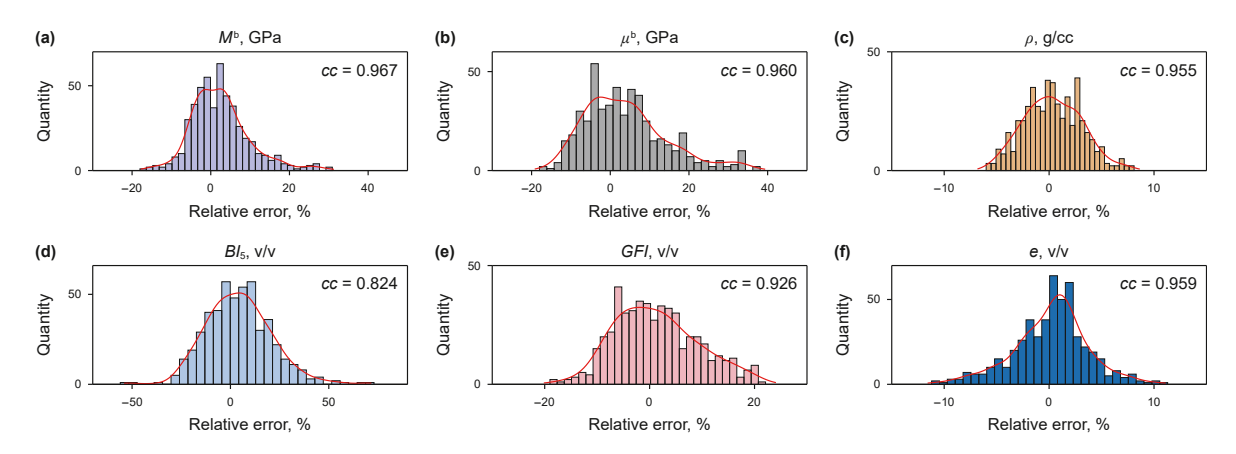
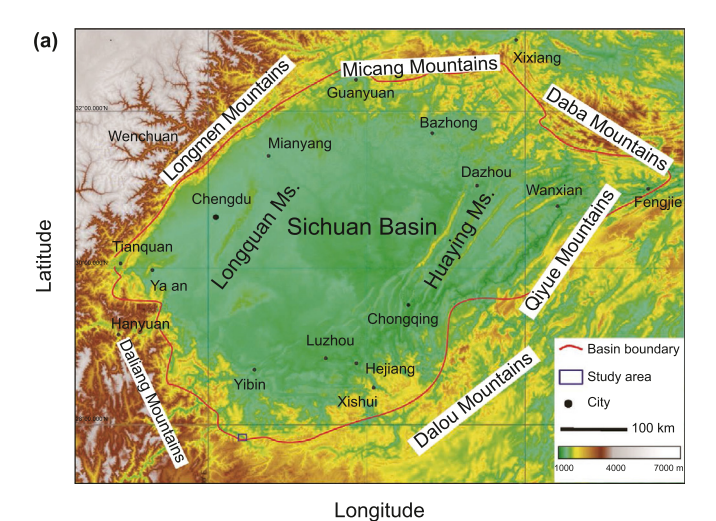


Fig. 21. Histogram of the relative error statistics of the noisy inversion results in Fig. 19, where (**a**) is the P-wave modulus M^b , (**b**) is the S-wave modulus μ^b , (**c**) is the density ρ , (**d**) is the brittleness index BI_5 , (**e**) is the fracture gas indication factor GFI and (**f**) is the fracture density e, with cc denoting the correlation coefficient and the red line denoting the density fitting curve.

are performed based on the prediction workflow shown in Fig. 12. We extracted and stacked an arbitrary survey line profile from the OVT-domain seismic data at various incident angles following the fracture development azimuth and perpendicular to the fracture azimuth, with the central incident angles of 5° (0– 10°), 15°

 $(10-20^\circ)$, and 25° $(20-30^\circ)$, and with a maximum time range of 1520–1800 ms, as shown in Fig. 24, where the black vertical lines represent the paths of Well A. The small ticks on the paths represent the interval tops interpreted at the well in Fig. 9, namely, T_1 , T_2 , and T_3 in order. We mark the fractured destination reservoir section



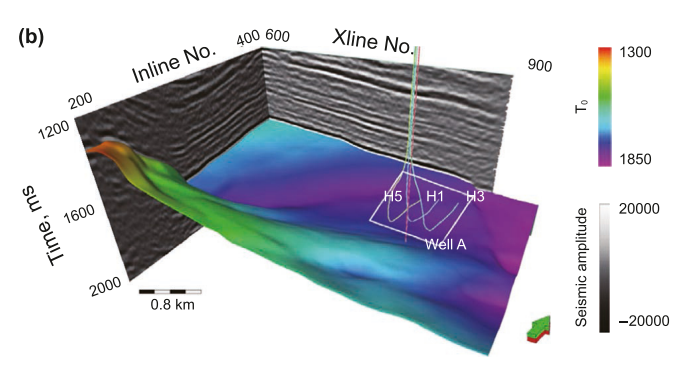


Fig. 22. The location and data information of the actual work area, where (**a**) is the location of the work area, and (**b**) is the data situation, including the seismic data and locations of the Wufeng Formation shale basement and vertical Well A (Lin et al., 2022).

from T_2 to T_3 in yellow on the Well A paths. Then the different azimuthal seismic data with the same incident angle are used to yield the azimuthal difference seismic data, as shown in Fig. 25. The well data in Fig. 9 are interpolated, extrapolated, and low-pass filtered to produce low-frequency initial models of the parameters in Fig. 26, which helps to supplement the background information and improve the inversion stability.

Fig. 27 shows the inversion results of the isotropic elastic parameters and the anisotropic fracture parameters, which are the P-wave modulus M^b , S-wave modulus μ^b , density ρ , brittleness index BI_5 , fracture gas indication factor GFI, and fracture density e, in which it can be recognized that the P-wave modulus and the S-wave modulus are relatively low in the target layer. The calculated brittleness index demonstrates an abnormally high value in the fractured reservoir sections indicating that the brittleness of the shale at the reservoir location is favorable for effective fracture stimulation.

As shown for Well A in Fig. 9, we have considered the locations with fracture gas indication factors greater than 0.06 as gas-rich locations and those with fracture densities greater than 0.04 as fracture development locations. The fracture gas indication factor *GFI* in Fig. 27(e) exhibits a high value in the reservoir location, indicating high fracture gas contents. The fracture density in Fig. 27(f) is also high in the destination layer, indicating fracture development in the shale reservoir. Fig. 28 represents the prestack inversion results of the elastic and fracture parameters for a single trace at the location of Well A, where the red-marked inversion results are in better agreement with the black-marked actual well

curves, which indicates the reasonableness of the inversion results. In comparison, the isotropic parameter inversion results in Fig. 28(a)—(c) are better than the weakly anisotropic parameter inversion results in Fig. 28(e) and (f), which is attributed to the marginal contribution to the PP-wave reflection coefficient. However, it is noticeable that the fracture parameters in Fig. 28(e) and (f), which utilize the azimuthal amplitude difference seismic data in advantage of the split-component inversion strategy demonstrate high values in the target layer location with a generally consistent overall trend. The statistics of the inversion results for Well A in Fig. 29 indicate that the inversion accuracy of the isotropic parameters is superior to that of the anisotropic parameters. At the same time, the correlation coefficients suggest that the inversion results of all the parameters are all fundamentally credible.

Ultimately, to predict the spatial development characteristics of fractured gas-bearing shale reservoirs, we conduct prestack inversion with 5D seismic data. Fig. 30 illustrates the layer slices extracted along the bottom of the Wufeng Formation shale bedding, where the black dots represent the position of the vertical Well A. The optimum brittleness index in Fig. 30(a) is distributed around Well A, with the expected high values indicating better shale brittleness. The fracture density in Fig. 30(c) exhibits high values in Well A, with surrounding fracture development, and the integrity of the fractures demonstrates a northeast-southwest orientation, which matches better with fracture orientation interpreted from the FMI images in Fig. 23(c). In addition, we can identify the scale of fracture gas development from Fig. 30(b). The fracture gas is enriched around vertical Well A. and there appears to be a relative association between the fracture gas development and the fracture density from southwest to northeast. Geological faults, as shown in Fig. 30(d) for the artificial fault interpretation result in F₁ generally induce more adjacent zones of microfracture aggregation, with relatively distinct waveform phase misalignments on seismic stacked profiles as shown by the green arrows in Fig. 30(e). The negative amplitude anomalies of the common depth point (CDP)-stacked seismic data in the bottom slices of the target layer indicate the approximate location of fault F_1 in Fig. 30(f), and the location of the fault is precisely located in the seismic amplitude variance in Fig. 30(g). To summarize, the method proposed in this paper for predicting fracture density e, the fracture fluid indication factor GFI, and the optimum brittleness index BI₅ offers improved characterization of gas-bearing shale reservoirs. This provides valuable technical support for enhancing shale gas production.

4. Conclusions

In this article, based on the petrophysical modeling of shale reservoirs, we have optimized the best form of the brittleness index to characterize the difficulty of shale fragmentation for Well A in a work area in the Sichuan Basin, China, Subsequently, we defined a fracture gas indication factor GFI to quantitatively describe the location and extent of the gas enrichment in the fractures. Then, we derived a new linear PP-wave reflection coefficient for TTI media, which achieves the direct inversion of the fracture gas indication factor GFI and fracture density e using the anisotropic component of the OVT-domain seismic data and the elastic parameters. The systematic prediction of engineering sweet spots (with the fracture density e and brittleness index BI_5) and geologic sweet spots (with the fracture gas indication factor GFI) can be effectively carried out to increase hydraulic pressure production of shale gas. We have further obtained the following conclusions based on the results of our experimental modeling tests and practical applications.

 Regarding the preferred brittleness index, we initially employed the conventionally brittle mineral fractions for preliminary

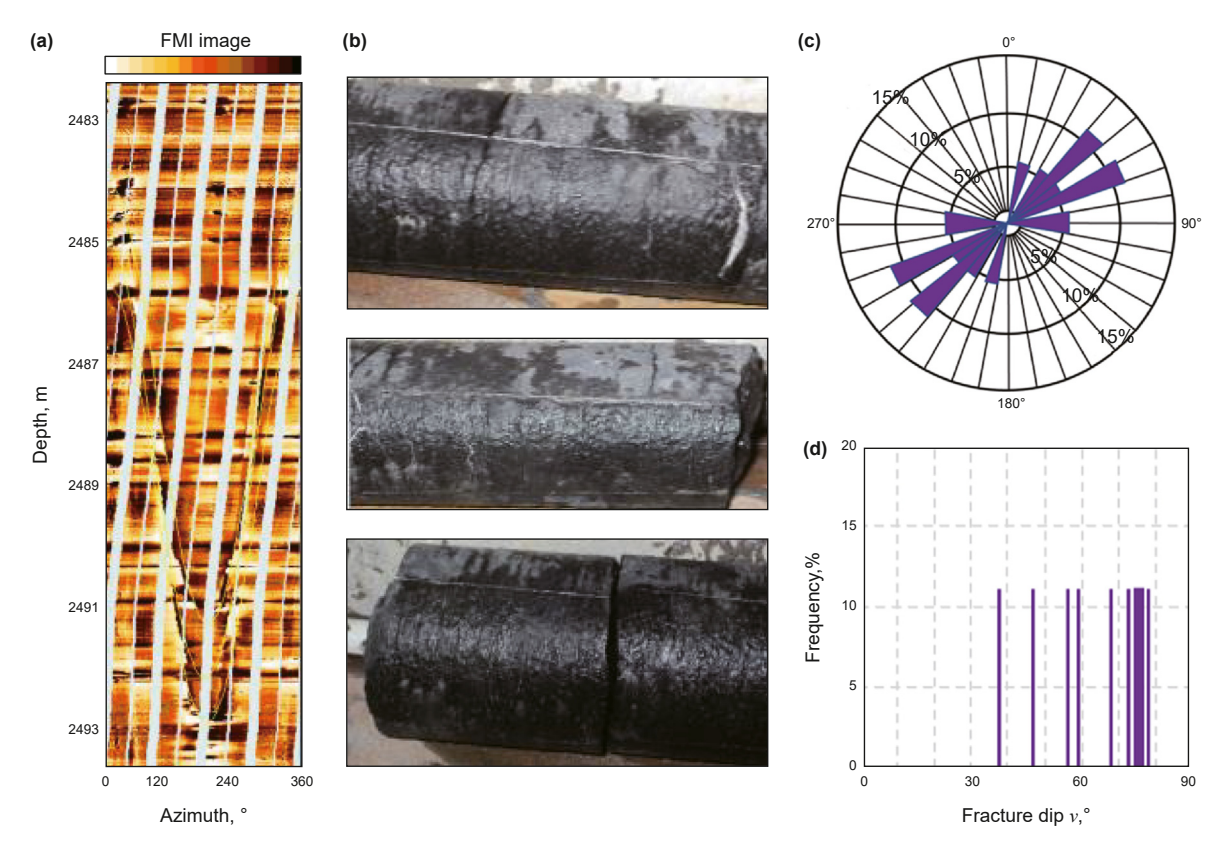


Fig. 23. The interpretation conclusion of fracture imaging in the target layer, where (a) is an FMI image, (b) is shale rock core images, (c) is the fracture orientation results, and (d) is the fracture inclination angle results.

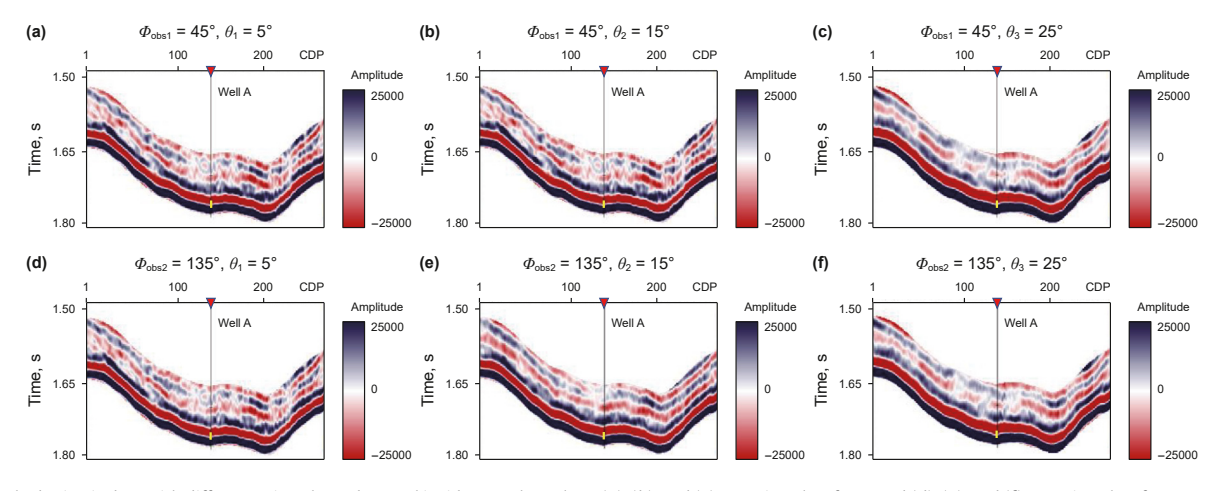


Fig. 24. Stacked seismic data with different azimuths and central incident angles, where (a), (b), and (c) are azimuths of 45°, and (d), (e), and (f) are azimuths of 135°, corresponding to central incident angles of 5°, 15°, and 25°, respectively.

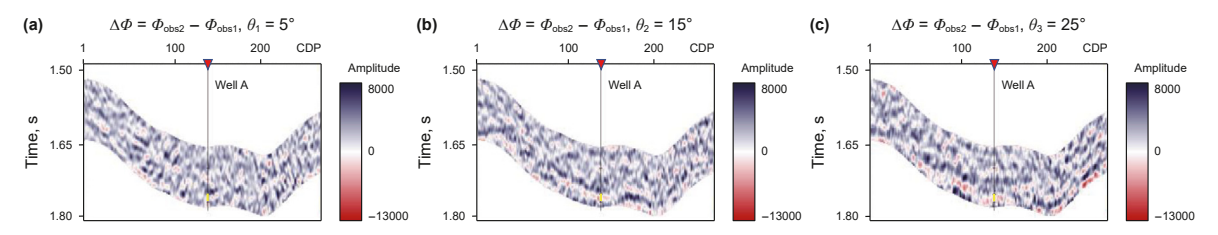


Fig. 25. Different azimuthal seismic amplitudes for different central incident angles, where (a), (b), and (c) are incident angles of 5°, 15°, and 25°, respectively.

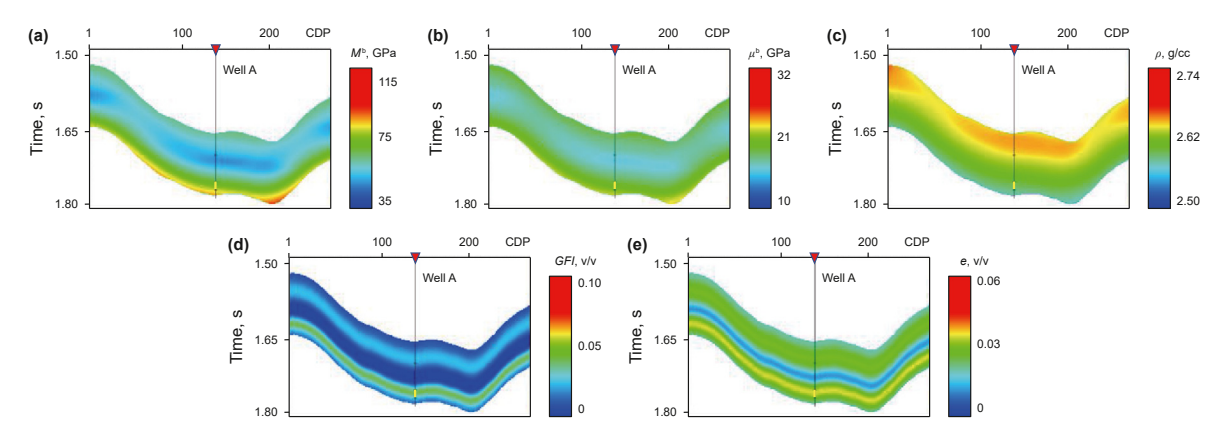


Fig. 26. Initial model of elastic and fracture parameters at a low frequency, where (**a**) is the P-wave modulus M^b , (**b**) is the S-wave modulus μ^b , (**c**) is the density ρ , (**d**) is the fracture gas indication factor *GFI* and (**e**) is the fracture density e.

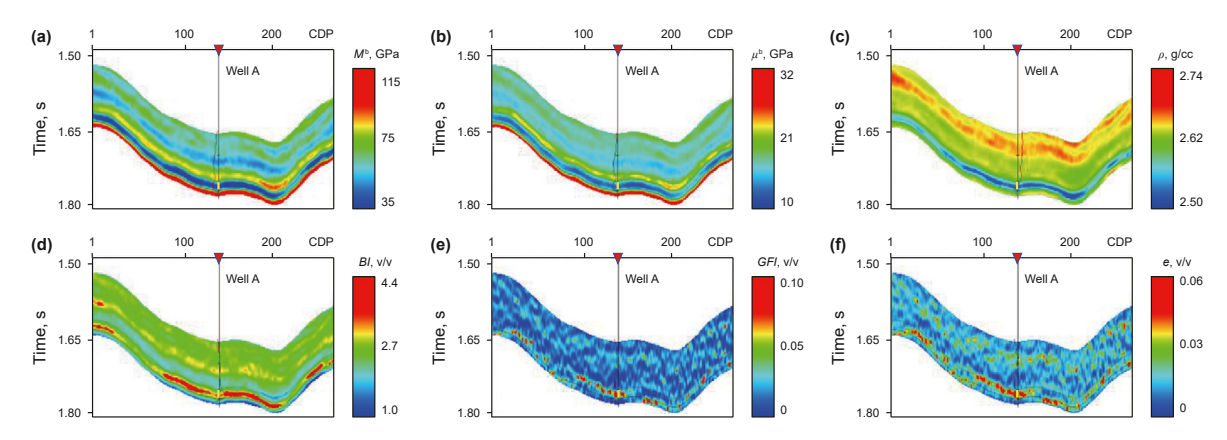


Fig. 27. Inversion results of isotropic background parameters and fracture parameters at an arbitrary survey line, where (**a**) denotes the P-wave modulus M^b , (**b**) denotes the S-wave modulus μ^b , (**c**) denotes the density ρ , (**d**) denotes the brittleness index BI_5 , (**e**) denotes the fracture gas indication factor GFI, and (**f**) denotes the fracture density e.

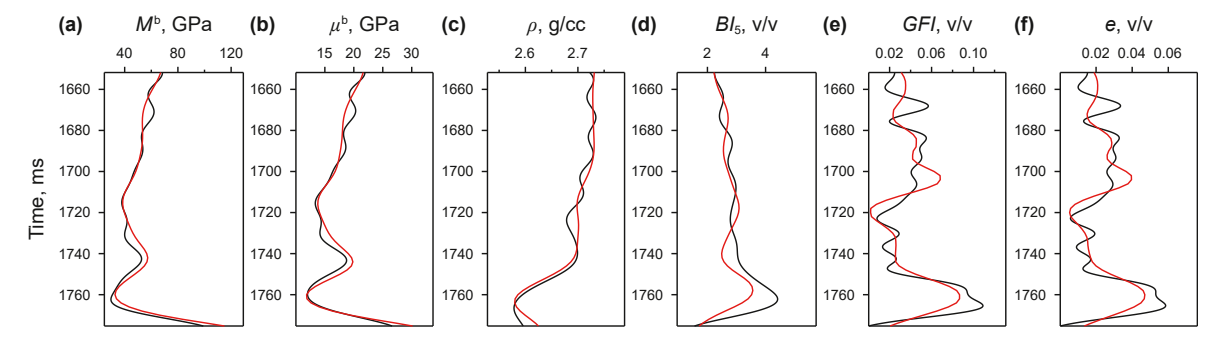


Fig. 28. Single-channel parameter inversion curves, where (**a**) is the P-wave modulus M^b , (**b**) is the S-wave modulus μ^b , (**c**) is the density ρ , (**d**) is the brittleness index BI_5 , (**e**) is the fracture gas indication factor *GFI* and (**f**) is the fracture density e, with the black lines representing the actual well curves, and the red lines representing the inversion curves.

selection. Then we compared the contributions of the property parameters, including porosity, gas saturation, and organic matter content, to the brittleness index through the petrophysical modeling method. Finally, we determined the optimal brittleness index with a high sensitivity to brittle minerals, shale porosity, and organic matter content. The efficiency of the petrophysical modeling of shale and the justification of the optimal brittleness index were also demonstrated with the interpretation of the actual logging curves of Well A.

We have defined a new fracture gas indication factor, GFI, whose petrophysical analyses demonstrate its high sensitivity to the fracture gas content and almost insensitivity to the fracture aspect ratio or fracture density. Considering the impacts of subsurface fracture inclination on seismic anisotropy, we derived a PP-wave reflection coefficient that incorporates the fracture gas indication factor *GFI* and the fracture density *e* for the TTI medium, which has not only achieves the direct inversion of the fracture parameters but also improves the accuracy of the weakly anisotropic and multiparameter inversion.

3) The results of theoretical modeling tests and practical applications demonstrated the effectiveness of the inversion algorithm with sparse constraints of the L_P quasinorm and the split-

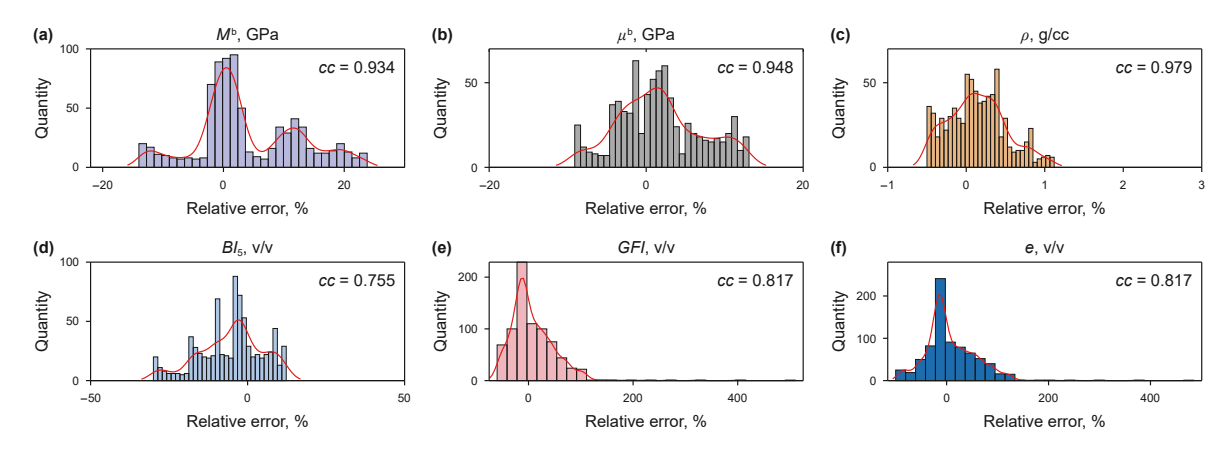


Fig. 29. Histogram of the relative error statistics of the actual inversion results in **Fig. 28**, where (**a**) is the P-wave modulus M^b , (**b**) is the S-wave modulus μ^b , (**c**) is the density ρ , (**d**) is the brittleness index BI_5 , (**e**) is the fracture gas indication factor GFI and (**f**) is the fracture density ρ , with ρ denoting the correlation coefficient and the red lines denoting the density fitting curves.

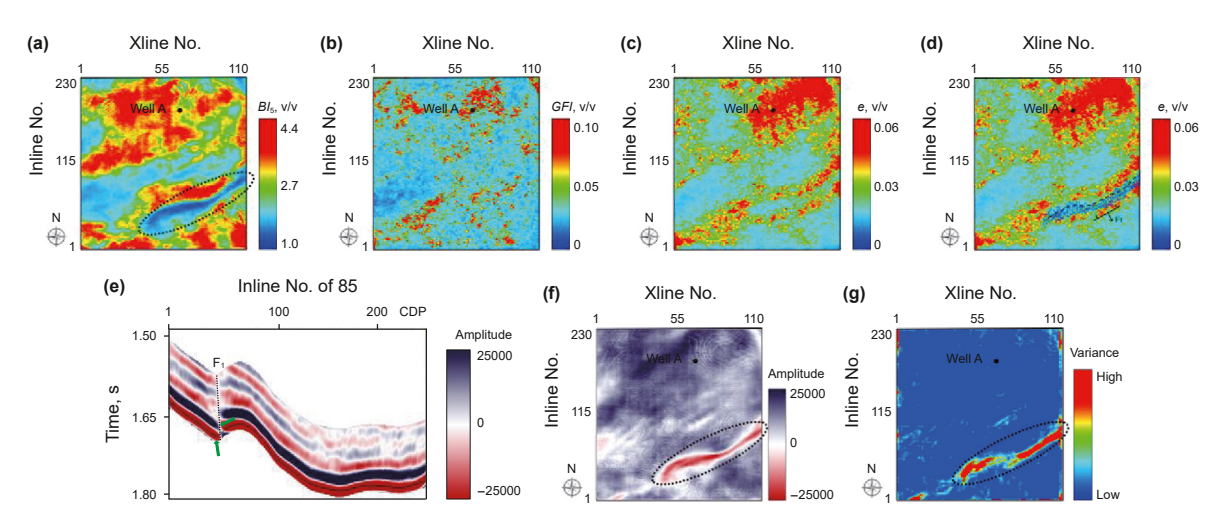


Fig. 30. Slices with the optimal brittleness index and fracture parameters along the bottom of the destination layer and associated interpretative conclusions, where (a) denotes the brittleness index Bl_5 , (b) denotes the fracture gas indication factor GFl, (c) denotes the fracture density e, (d) denotes the fracture density e with the geological fault F_1 , (e) denotes the amplitude slice of the CDP-stacked seismic date, (f) denotes the prediction of faulting results based on seismic amplitude variance, and (g) denotes the variance attribute.

component inversion strategy introduced in this article. These research achievements can effectively predict the brittleness index, fracture density, and fracture gas in fractured gas-bearing shale reservoirs, which is significant for practical production.

In addition, there are some limitations and improvements in our study. The brittleness index is the indirect result of the elastic parameter prediction, which is susceptible to unavoidable and indirect errors with low-SNR seismic data, but subsequent research could be carried out to realize the direct prediction of the brittleness index. The fracture inclination angles were obtained from the FMI interpretation on the well, and we could further study how to invert the fracture dips based on anisotropy theory.

CRediT authorship contribution statement

Yun Zhao: Writing — original draft, Methodology, Funding acquisition, Formal analysis, Data curation, Conceptualization. **Xiao-Tao Wen:** Writing — review & editing. **Chen-Long Li:** Supervision. **Yang Liu:** Software, Investigation. **Chun-Lan Xie:** Validation, Supervision.

Declaration of competing interest

The authors declare that they have no known competing financial interests or personal relationships that could have appeared to influence the work reported in this paper.

Acknowledgments

This study was financially supported by the Sichuan Science and Technology Program (Grant No. 2023ZYD0158) and the National Natural Science Foundation of China (Grant Nos. 42304147 and 42304076). We sincerely appreciate all the authors who contributed to the writing and revision of the article. We also thank the editors and reviewers for their valuable and constructive suggestions.

References

Backus, G.E., 1962. Long-wave elastic anisotropy produced by horizontal layering.
 J. Geophys. Res. 67 (11), 4427–4440. https://doi.org/10.1029/J20671011P04427.
 Bakulin, A., Crechka, V., Tsvankin, I., 2000. Estimation of fracture parameters from reflection seismic data—Part I: HTI model due to a single fracture set. Geophysics 65 (6), 1708–2018. https://doi.org/10.1190/1.1444863.

Berryman, J.G., 1980. Long-wavelength propagation in composite elastic media. J. Acoust. Soc. Am. 68 (6), 1800. https://doi.org/10.1121/1.385171.

- Berryman, J.G., 1995. Mixture Theories for Rock Properties. Rock Physics & Phase Relations, American. https://doi.org/10.1029/RF003p0205.
- Boyd, S., Parikh, N., Chu, E., et al., 2011. Distributed optimization and statistical learning via the alternating direction method of multipliers. Found. Trends Mach. Learn. 3 (1), 1–122. https://doi.org/10.1561/2200000016.
- Brown, R.J.S., Korringa, J., 1975. On the dependence of the elastic properties of a porous rock on the compressibility of the pore fluid. Geophysics 40 (4), 593–701. https://doi.org/10.1190/1.1440551.
- Budiansky, B., 1965. On the elastic moduli of some heterogeneous materials.

 J. Mech. Phys. Solid. 13 (4), 223–227. https://doi.org/10.1016/0022-5096(65)
- Chen, H.Z., Ji, Y.X., Innanen, K.A., 2018. Estimation of modified fluid factor and dry fracture weaknesses using azimuthal elastic impedance. Geophysics 83 (1), WA73—WA88. https://doi.org/10.1190/geo2017-0075.1.
- Chen, H.Z., Yin, X.Y., Qu, S.L., et al., 2014a. AVAZ inversion for fracture weakness parameters based on the rock physics model. J. Geophys. Eng. 11 (6), 1742–2132. https://doi.org/10.1088/1742-2132/11/6/065007.
- Chen, J.J., Zhang, G.Z., Chen, H.Z., et al., 2014b. The construction of shale rock physics effective model and prediction of rock brittleness. SEG Tech. Progr. Expand. Abstr. https://doi.org/10.1190/segam2014-0716.1.
- Euhanna, G., André, T., Iman, S., et al., 2015. Optimal parameter selection for the alternating direction method of multipliers (ADMM): quadratic problems. IEEE Trans. Automat. Control 60 (3), 644–658. https://doi.org/10.1109/TAC.2014.2354892.
- Ge, Z.J., Pan, S.L., Li, J.Y., 2020. Seismic AVOA inversion for weak anisotropy parameters and fracture density in a monoclinic medium. Appl. Sci. 10 (15), 5136–5152. https://doi.org/10.3390/app10155136.
- Goodway, B., Chen, T., Downton, J., 1997. Improved AVO fluid detection and lithology discrimination using Lamé petrophysical parameters; "λρ", "μρ", "λμ fluid stack", from P and S inversions. SEG Tech. Progr. Expand. Abstr. https://doi.org/10.1190/1.1885795.
- Guo, Z.Q., Chapman, M., Li, X.Y., 2012. A shale rock physics model and its application in the prediction of brittleness index, mineralogy, and porosity of the Barnett Shale. SEG Tech. Progr. Expand. Abstr. https://doi.org/10.1190/segam2012-07771
- Hill, R., 1952. The elastic behaviour of a crystalline aggregate. Proc. Phys. Soc. A, 349–354. https://doi.org/10.1088/0370-1298/65/5/307.
- Huang, G.T., Ba, J., Gei, D., et al., 2022. A matrix-fracture-fluid decoupled PP reflection coefficient approximation for seismic inversion in tilted transversely isotropic media. Geophysics 87 (6), M275–M292. https://doi.org/10.1190/geo2.021-0631.1.
- Hudson, J.A., 1980. Overall properties of a cracked solid. Math. Proc. Camb. Phil. Soc. 88 (2), 371–384. https://doi.org/10.1017/S0305004100057674.
- Jech, J., Pšenčik, I., 1989. First-order perturbation method for anisotropic media. Geophys. J. Int. 99 (2), 369–376. https://doi.org/10.1111/j.1365-246X.1989.tb01694.x.
- Kuster, G.T., Toksöz, M.N., 1974. A Velocity and attenuation of seismic waves in two-phase media. Geophysics 39 (5), 587–606. https://doi.org/10.1190/1.1440450.
- Lin, K., Zhang, B., Zhang, J.J., et al., 2022. Predicting the azimuth of natural fractures and in situ horizontal stress: a case study from the Sichuan Basin, China. Geophysics 87 (1), B9—B22. https://doi.org/10.1190/geo2020-0829.1.
- Luo, T., Feng, X., Guo, Z.Q., et al., 2019. Seismic AVAZ inversion for orthorhombic shale reservoirs in the Longmaxi area, Sichuan. Appl. Geophys. 16 (2), 185–198. https://doi.org/10.1007/s11770-019-0759-0.
- Mavko, G., Mukerji, T., Dvorkin, J., 2009. The Rock Physics Handbook: Tools for Seismic Analysis of Porous Media, second ed. Cambridge University Press, New York, https://doi.org/10.1017/CB09780511626753.
- Pan, X.P., Li, L., Zhou, S.X., et al., 2021. Azimuthal amplitude variation with offset parameterization and inversion for fracture weaknesses in tilted transversely isotropic media. Geophysics 86 (1), C1–C18. https://doi.org/10.1190/geo2019-0215.1.
- Pan, X.P., Zhang, G.Z., Chen, J.J., 2020. The construction of shale rock physics model and brittleness prediction for high-porosity shale gas-bearing reservoir. Petrol. Sci. 17 (3), 658–670. https://doi.org/10.1007/s12182-020-00432-2.
- Pan, X.P., Zhang, G.Z., 2018. Estimation of fluid indicator and dry fracture compliances using azimuthal seismic reflection data in a gas-saturated fractured reservoir. J. Pet. Sci. Eng. 167, 737–751. https://doi.org/10.1016/j.petrol.2018.04.054.
- Pointer, T., Liu, E., Hudson, J.A., 2000. Seismic wave propagation in cracked porous media. Geophys. J. Int. 142 (1), 199–231. https://doi.org/10.1046/j.1365-246x.2000.00157.x.
- Qian, K.R., He, Z.L., Liu, X.W., et al., 2017. Analyzing the anisotropic characteristics of shale brittleness based on shale rock physics model. SEG Tech. Progr. Expand. Abstr. https://doi.org/10.1190/segam2017-17539402.1.

Qin, Z.Y., Wen, X.T., Zhou, D.Y., et al., 2022. Inversion method of elastic and fracture parameters of shale reservoir with a set of inclined fractures. IEEE Trans. Geosci. Rem. Sens. 60, 1–13. https://doi.org/10.1109/TGRS.2021.3138750.

- Reuss, A., 1929. Berechnung der fleissgrenze von mischkristallen auf grund der plastizitats bedingung für einkrisalle. Zamm-zeitschrift Fur Angewandte Mathematik Und Mechanik 9 (1), 49–58. https://doi.org/10.1002/zamm.19290090104.
- Rickman, R., Mullen, M., Petre, E., et al., 2008. A practical use of shale petrophysics for stimulation design optimization: All shale plays are not clones of the Barnett shale. SPE Annual Technical Conference & Exhibition Society of Petroleum Engineers. https://doi.org/10.2118/115258-MS.
- Schoenberg, M., 1980. Elastic wave behavior across linear slip interfaces. J. Acoust. Soc. Am. 68, 1516–1521. https://doi.org/10.1121/1.385077.
- Schoenberg, M., Sayers, C.M., 1995. Seismic anisotropy of fractured rock. Geophysics 60 (1), 19–307. https://doi.org/10.1190/1.1443748.
- Schoenberg, M., Douma, J., 1998. Elastic wave propagation in media with parallel fractures and aligned cracks. Geophys. Prospect. 36 (6), 571–590. https:// doi.org/10.1111/j.1365-2478.1988.tb02181.x.
- Sharma, R.K., Chopra, S., 2012. New attribute for determination of lithology and brittleness. SEG Tech. Progr. Expand. Abstr. https://doi.org/10.1190/segam2012-1389.1.
- Shaw, R.K., Sen, M.K., 2004. Born integral, stationary phase and linearized reflection coefficients in weak anisotropic media. Geophys. J. Int. 158 (1), 225–238. https://doi.org/10.1111/j.1365-246X.2004.02283.x.
- Smith, G.C., 2003. The fluid factor angle and the crossplot angle. SEG. Tech. Program. Expand. Abstr. pp. 26–31. https://doi.org/10.1190/1.1817679.
- Thomsen, L., 1995. Elastic anisotropy due to aligned cracks in porous rock. Int. J. Rock Mech. Min. Sci. 33 (5), A211. https://doi.org/10.1111/j.1365-2478.1995.tb00282.x.
- Walton, G., Hedayat, A., Kim, E., et al., 2017. Post-yield strength and dilatancy evolution across the brittle-ductile transition in Indiana limestone. Rock Mech. Rock Eng. 50 (7), 1691–1710. https://doi.org/10.1007/s00603-017-1195-1.
- Wang, J., Du, J.H., Li, W.P., et al., 2023. Brittleness index evaluation of gas-bearing sandstone under triaxial compression conditions. Geomech. Geophys. Geo. 9 (1), 160. https://doi.org/10.1007/s40948-023-00713-1.
- Wood, A.B., Lindsay, R.B., 1956. A Textbook of Sound. Phys. Today 9 (11), 37. https://doi.org/10.1063/1.3059819.
- Xie, J.Y., Zhang, J.J., Fang, Y.P., et al., 2023. Quantitative evaluation of shale brittleness based on brittle-sensitive index and energy evolution-based fuzzy analytic hierarchy Process. Rock Mech. Rock Eng. 56 (4), 3003–3021. https://doi.org/ 10.1007/s00603-022-03213-y.
- Xue, J., Gu, H.M., Cai, C.G., 2017. Model-based amplitude versus offset and azimuth inversion for estimating fracture parameters and fluid content. Geophysics 82 (2), 1MA–Z12. https://doi.org/10.1190/geo2016-0196.1.
- Yin, L.J., Yin, X.Y., Zong, Z.Y., et al., 2020. A new rock physics model method for shale on the theory of micro-nanopores. Chin. J. Geophys. 63 (4), 1642–1653. https:// doi.org/10.6038/cjg2020M0448 (in Chinese).
- Yu, S.H., Zong, Z.Y., Li, K., 2023. Rock physics and seismic reflectivity parameterization for amplitude-variation-with-angle inversion of low-maturity source rocks. Geophysics 88 (6), R703—R719. https://doi.org/10.1190/geo2022-0734.1.
- Zeng, Y.J., Zong, Z.Y., Pan, X.P., 2023. Azimuthal seismic inversion for effective elastic orthorhombic anisotropic media formed by two orthogonal sets of vertical fractures. IEEE Trans. Geosci. Rem. Sens. 61, 1. https://doi.org/10.1109/TGRS.2023.3314688.
- Zhang, G.Z., Chen, J.J., Chen, H.Z., et al., 2015a. Prediction for in-situ formation stress of shale based on rock physics equivalent model. Chin. J. Geophys. 58 (6), 2112–2122. https://doi.org/10.6038/cjg20150625 (in Chinese).
- Zhang, G.Z., Pan, X.P., Li, Z.Z., et al., 2015b. Seismic fluid identification using a nonlinear elastic impedance inversion method based on a fast Markov chain Monte Carlo method. Petrol. Sci. 12, 406–416. https://doi.org/10.1007/s12182-015-0046-5.
- Zhao, L., Lin, K., Wen, X.T., et al., 2023. Anisotropic total variation pre-stack multitrace inversion based on Lp norm constraint. J. Pet. Sci. Eng. 220 (Part B), 111212. https://doi.org/10.1016/j.petrol.2022.111212.
- Zhao, W.T., Jing, T.Y., Bai, J.Y., et al., 2018. AVAZ inversion method based on full azimuth seismic data. Prog. Geophys. 33 (3), 1184–1189. https://doi.org/10.6038/pg2018BB0180 (in Chinese).
- Zong, Z.Y., Man, J., Xu, M.M., 2020. Influencing factor analysis of the elastic properties of shale with rock-physical model including pressure effects. Interpretation 8 (3), T515–T524. https://doi.org/10.1190/INT-2019-0128.1.
- Zong, Z.Y., Yin, X.Y., Wu, G.C., 2012. AVO inversion and poroelasticity with P- and S-wave moduli. Geophysics 77 (6), N17–N24. https://doi.org/10.1190/geo2011-0214.1.
- Zuo, Y.H., Zong, Z.Y., Li, K., 2023. Direct inversion for shale brittleness index using a delayed rejection adaptive Metropolis-Markov chain Monte Carlo method. Geophysics 88 (5), M225–M237. https://doi.org/10.1190/geo2022-0567.1.